Center-of-Gravity-Based Approach for Modeling Dynamics of Multisection Continuum Arms

Isuru S. Godage, *Member, IEEE*, Robert J. Webster, III, *Senior Member, IEEE*, and Ian D. Walker, *Fellow, IEEE*

***Abstract*—Multisection continuum arms offer complementary characteristics to those of traditional rigid-bodied robots. Inspired by biological appendages, such as elephant trunks and octopus arms, these robots trade rigidity for compliance and accuracy for safety and, therefore, exhibit strong potential for applications in human-occupied spaces. Prior work has demonstrated their superiority in operation in congested spaces and manipulation of irregularly shaped objects. However, they are yet to be widely applied outside laboratory spaces. One key reason is that, due to compliance, they are difficult to control. Sophisticated and numerically efficient dynamic models are a necessity to implement dynamic control. In this paper, we propose a novel numerically stable center-of-gravity-based dynamic model for variable-length multisection continuum arms. The model can accommodate continuum robots having any number of sections with varying physical dimensions. The dynamic algorithm is of $\mathcal{O}(n^2)$ complexity, runs at 9.5 kHz, simulates six to eight times faster than real time for a three-section continuum robot, and, therefore, is ideally suited for real-time control implementations. The model accuracy is validated numerically against an integral-dynamic model proposed by the authors and experimentally for a three-section pneumatically actuated variable-length multisection continuum arm. This is the first sub-real-time dynamic model based on a smooth continuous deformation model for variable-length multisection continuum arms.**

***Index Terms*—Center of gravity (CoG), continuum arms, dynamics, real time.**

I. Introduction

RIGID-BODIED robots have been the backbone of the robotic industrial revolution, which has not only significantly improved throughput, but also relieved humans of most of the mundane, repetitive, dangerous, and dirty tasks of assembly lines. Rigid-linked industrial robots have high payload capacity and precision superior to human capabilities. However, the lack of compliance of rigid robots renders them dangerous, and therefore, industrial robot task spaces are often restricted of human presence. In addition, due to the structural rigidity, they are poorly adaptable to environmental interaction and yield poor performance in unstructured environments [1]. There is currently great interest in robots that work cooperatively with humans [2], which implies a need for inherently human-safe robotic manipulators. Continuum robots have been proposed as a potential solution to serve niche applications, where adaptability, compliance, and human safety are critical [3]. In this paper, we refer to continuum robots as those robotic structures that lack rigid frames and generate motion through smooth continuous structural deformation, such as the robots reported in [4]–[9].

Continuum arms are inspired by biological appendages such as elephant trunks and octopus arms. Such muscular structures are highly deformable and able to achieve complex geometrical shapes. Despite being made entirely out of muscles, they demonstrate compelling benchmarks in terms of forces and precision of operation [12]–[16]. Often constructed from elastic material, continuum arms aim to imitate such behavior by generating complex smooth geometric shapes through structural deformation. The smaller continuum robots target operation in smaller spaces such as inside human bodies during minimally invasive surgeries [17] and are actuated by elastic tubes or tendons. The larger variants constructed to handle macro or human body scale objects are often powered by pneumatic muscle actuators (PMAs). PMAs, also known as McKibben actuators, have a number of desirable features, such as ease of design, fabrication, and high power-to-weight ratio, and therefore are sought after in continuum arm designs. In this paper, we focus on PMA-powered variable-length multisection continuum arms. There are several key features common to this type of manipulator. Unlike tendon-actuated continuum arms, they are fabricated by serially stacking continuum sections, where each continuum section consists of multiple PMAs (typically three, though four actuators are also possible [6]), and are capable of generating omnidirectional bending deformation independent of other sections. Since there are no backbones, continuum sections undergo axial length changes, extend or contract, depending on the PMA operation mode. Fig. 1 shows a couple of variable-length multisection continuum arm prototypes. Due to their unique mechanical characteristics, deriving mathematical models for these robots has been a challenge.

A. Prior Work on Dynamic Modeling of Continuum Arms

Early continuum-style (which are not truly continuum without continuously bending deformation) robots have been

Manuscript received November 3, 2018; accepted May 17, 2019. Date of publication June 27, 2019; date of current version October 1, 2019. This work was supported in part by the National Science Foundation under Grant IIS-1718755. This paper was recommended for publication by Associate Editor A. Degani and Editor P. Dupont upon evaluation of the reviewers' comments. *(Corresponding author: Isuru S. Godage.)*

I. S. Godage is with the School of Computing, DePaul University, Chicago, IL 60604 USA (e-mail: igodage@depaul.edu).

R. J. Webster, III is with the Department of Mechanical Engineering, Vanderbilt University, Nashville, TN 37212 USA (e-mail: robert.webster@vanderbilt.edu).

I. D.Walker is with the Department of Electrical and Computer Engineering, Clemson University, Clemson, SC 29634 USA (e-mail: iwalker@clemson.edu).

Color versions of one or more of the figures in this paper are available online at http://ieeexplore.ieee.org.

Digital Object Identifier 10.1109/TRO.2019.2921153

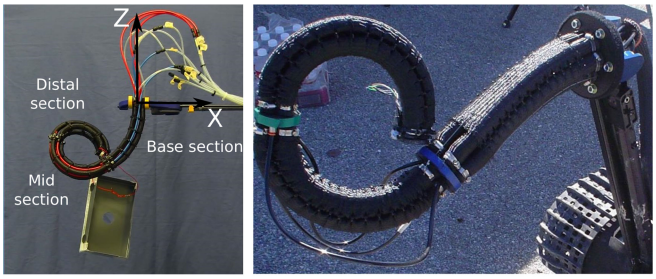

(a) (b)

Fig. 1. Examples of PMA-powered variable-length multisection continuum arms. (a) Continuum arm developed at the Italian Institute of Technology is used to validate the dynamic model proposed in this paper [10]. (b) OctArm-IV [11] continuum manipulator developed at Clemson University.

discretized rigid structures [18], [19] that mimicked smooth bending. The computational constraints that prevailed at the time motivated numerically efficient parametric or modal approaches [20]. However, such low-dimensional methods did not fully capture the complete task space and suffered from numerical instabilities [21]. Other early continuum-style robots and discrete-link dynamic models include [5], [14], [22].

Cosserat rod theory has been proposed to model quasi-statics of tendon actuated inextensible flexible backbone and concentric-tube continuum robots. The works in [6] and [23] model the dynamics of a multibending soft manipulator. But due to the complexity of deformable bodies, the methods reported inefficient simulation times. The work reported in [24] utilized elliptic integrals to develop kinematics and statics of miniature single continuum section. Kane's method was used in [25] to model the dynamics of a tendon-actuated continuum manipulator. The work in [26] validated a planar static Cosserat rod model for PMA-actuated variable-length multisection continuum arms.

Another avenue to derive equations of motion (EoMs) is to utilize energy-based methods such as the Lagrangian formulation. During operation, the relative displacement between points of a continuum body varies and thus limits the use of numerically efficient algorithms [27]. Theoretical models for inextensible rope-like mechanisms were proposed in [28], but continuum arms have multiple degrees of freedom (DoF).

The kinematic model reported in [29] laid the foundation for curve parametric models for variable-length continuum arms. Nonetheless, the use of circular arc parameters resulted in complex nonlinear terms and numerical instabilities for straight-arm poses to limit the model's extensibility for modeling dynamics. For an in-depth treatment of the limitations of curve parametric models, see [10]. An energy-based derivation of planar dynamic models for OctArm variable-length continuum manipulator [11] was reported in [30] and [31]. However, continuum arms are capable of spatial operation, and the models were not experimentally validated. In addition, the resulting EoM were nonlinear, complex, and of integral nature, and therefore numerically inefficient and unstable.

Prior work by the first author proposed a modal method to overcome the numerical instabilities and inefficiencies present in curve parametric models [32]. Therein, the terms of the homogeneous transformation matrix (HTM) of continuum sections were approximated by multivariate polynomials [10], [32], where the degree of polynomials could be chosen to meet desired error metrics. The model laid the foundation for formulating EoMs of variable-length continuum sections [33]–[35]. The extended recursive formulation was later validated for a variable-length multisection continuum manipulator [36], where the integral terms are presolved to improve numerical performance.

Numerically efficient (via rigid body dynamic algorithms) lumped models have also been applied for continuum robots. However, such models require a large number of discrete joints to approximate the deformation [14], [22], [37]. Some work has attempted to trade numerical efficiency for modeling accuracy by using relatively few rigid segments [38], [39]. However, such lumped parametric approaches lose unique features of continuum arms such as smooth bending.

The key motivation of this paper is to introduce a lumped model without betraying the continuous nature of the resulting expressions. Our prior work introduced a center of gravity (CoG)-based modeling approach for a single-section continuum arm [40], [41]. Therein, the EoMs were derived for a point mass at the CoG of the continuum section. Thus, instead of an integral formulation, the process resulted in a compact model and superior numerical efficiency. In the derivation process, due to the physical dimensions of the robot, we did not consider the angular kinetic energy, as the energy contribution was less than 3%. But this will not be the case for all continuum arms. Besides, the model was limited to a single-section continuum arm, where multisection continuum arms are required for performing useful tasks such as whole arm manipulation [42] and spatial trajectory tracking [32].

B. Contributions

In this paper, we extend and generalize our CoG-based spatial dynamic model derived for a single continuum section [41], evaluate against the integral dynamics proposed in [36] to verify the numerical accuracy and computational efficiency, and validate the model against spatial dynamic responses of the prototype arm shown in Fig. 1(a). Beyond our prior work reported in [36], [40], and [41], the proposed dynamic model:

1) theoretically accommodates variable-length multisection continuum arms with any number of sections and a wide range of length and radii combinations;
2) considers both linear and angular kinetic energies of a continuum arm at the CoG for better energy accuracy;
3) achieves energy matching via a series of energy-shaping coefficients that are constant for any variable-length multisection continuum arm;
4) employs the results from [36] to systematically and recursively derive the EoM;
5) demonstrates $\mathcal{O}\left(n^2\right)$ complexity for the first time for a dynamic model for a three-section continuum arm based on continuous (nondiscretized) deformation representation;
6) runs at 9.5 kHz (step execution rate);

TABLE I
NOMENCLATURE OF MATHEMATICAL SYMBOLS

Symbol	Definition
i	Continuum section index$^\sharp$.
$\overline{[]}$	Refers to the center of gravity-related terms
r_i, L_i,l_{ij}	Radius, original length, and jth actuator length change
$\boldsymbol{q}$,$\boldsymbol{q}_i$,$\boldsymbol{q}^i$	Complete, ith, and up to ith section joint-space vector*
$\{O\}$,$\{O_i\}$,$\{O_i'\}$	Task, base, and moving coordinate frames
$\mathbf{T}_i$,$\boldsymbol{p}_i$,$\mathbf{R}_i$	HTM‡, position, and rotation matrices relative to $\{O_i\}$
$\mathbf{T}^i$,$\boldsymbol{p}^i$,$\mathbf{R}^i$	HTM, position, and rotation matrices relative to $\{O\}$
ξ_i	Scalar to define $\{O_i'\}$ along the continuum section
m_i	Mass of continuum section
$\mathcal{K}$, $\mathcal{K}_i$	Total and ith section kinetic energy
$\mathcal{K}_i^\omega$, $\mathcal{K}_i^v$	Angular and linear kinetic energies of continuum section
β_j^ω, β_j^v	Energy shaping coefficients $\forall j \in \{1,2,3\}$
$\mathcal{P}$, $\mathcal{P}_i$	Total and ith section potential energy
$\mathcal{M}_i^v$, $\mathcal{M}_i^\omega$	Disc linear and angular inertia matrices
$\mathbf{M}$, $\mathbf{C}$	Complete inertia and Coriolis/Centrifugal matrices
$\mathbf{M}_i^v$, $\mathbf{M}_i^\omega$	Generalized linear and angular inertia matrices
$\mathbf{C}_i^v$, $\mathbf{C}_i^\omega$	Linear, angular Coriolis/Centrifugal force matrices
$\boldsymbol{G}$,$\boldsymbol{G}_i$	Complete, ith section conservative force vectors
$\mathbf{J}_i^v$,$\mathbf{H}_i^v$	Linear velocity Jacobian and Hessian w.r.t to $\{O_i'\}$
$\mathbf{J}_i^\Omega$,$\mathbf{H}_i^\Omega$	Angular velocity Jacobian and Hessian w.r.t to $\{O_i'\}$
$\mathbf{K}_i^e$	Elastic stiffness coefficient matrix
$\boldsymbol{\tau}$	Complete input force vector in the joint-space
$\mathbf{I}_3$	Rank 3 identity matrix

$^\sharp$ Subscript i represents the ith continuum section parameters, whereas superscript stands for terms associated with up to the ith continuum section.
*Lowercase, boldface italics (i.e., $\boldsymbol{q}_j$) denote vectors and regular lowercase italics (i.e., l_{ij}or h) denote vector/matrix elements or constants. Matrices are denoted by boldface uppercase letters (i.e., $\mathbf{T}$, $\mathbf{M}_i^\omega$).
‡ Homogeneous transformation matrix (HTM).
All quantities are represented in metric units.

TABLE II
NOMENCLATURE OF MATHEMATICAL OPERATORS

Operator	Definition
$(\ )_{,\boldsymbol{q}}$	Partial derivative with respect to elements of $\boldsymbol{q}$ along the dimension of $\boldsymbol{q}$. Eg. if $\boldsymbol{q} \in \mathbb{R}^{n\times 1}$ and $\mathbf{A} \in \mathbb{R}^{u\times v}$, then $\mathbf{A}_{,\boldsymbol{q}} \in \mathbb{R}^{nu\times v}$ and $\mathbf{A}_{,\boldsymbol{q}^T} \in \mathbb{R}^{u\times nv}$ respectively.
$(\ )^\vee$	Forms the velocity vector from skew-symmetric angular velocity matrix
$\int$	Integration from 0 to 1 with respect to ξ_i
$\mathbb{T}_2$	Trace operator (involving only the first two diagonal elements) on a 3×3 matrix or sub-matrix

7) achieves sub-real-time dynamic simulation in the MATLAB Simulink environment.

Therefore, the proposed model unifies the ideas of lumped parametric approaches of discrete rigid-bodied robotics and continuous (integral) approaches of continuum robotics and is expected to lay a strong numerical and algorithmic foundation for implementing real-time dynamic control schemes.

II. KINEMATICS OF CENTERS OF GRAVITY

A. System Model and Assumptions

Tables I and II list the nomenclatures of mathematical symbols and operators employed in this paper. Fig. 2(a) shows the schematic of a multisection continuum arm with $n \in \mathbb{Z}^+$ sections. The sections are numbered starting from the base continuum section (index 1) attached to the task-space coordinate system, $\{O\}$. Any ith continuum section [see Fig. 2(b)] is assumed to be actuated by three extending PMAs, which are mounted on plates situated at either end at $r_i \in \mathbb{R}^+$ distance

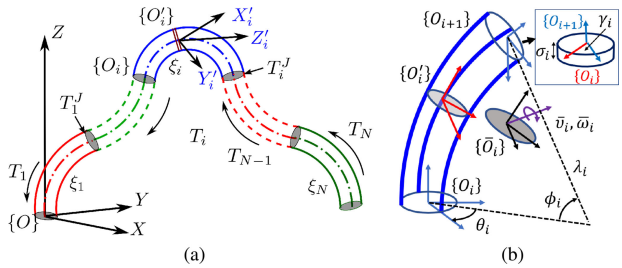

Fig. 2. (a) Schematic of a multisection continuum arm. (b) Schematic of an infinitesimally thin slice the CoG of any ith continuum section. The linear (σ_i) and angular (γ_i) offsets at continuum sections joints are also shown.

from the neutral axis and $\frac{2\pi}{3}$ rad apart. Let the unactuated length of PMAs be $L \in \mathbb{R}^+$, the maximum length change $l_{\max}$, and the joint-space vector of the continuum section, $\boldsymbol{q}_i = [l_{i1}, l_{i2}, l_{i3}]^T$, where $l_{ij} \in [0, l_{\max}]\ \ \forall j \in \{1,2,3\}$. The joint where the $(i+1)$ th continuum section is attached introduces $\sigma_i \in \mathbb{R}_0^+$ linear displacement along and $\gamma_i \in \mathbb{R}_0$ angular displacement about the $+Z$-axis of $\{O_i\}$. As the PMAs are constrained to maintain r_i clearance normal to the neutral axis, differential length changes cause the section to bend or extend (when length changes are equal) [11]. The subsequent derivations rely on the assumptions that the continuum sections bend in circular arc shapes, have no backbone, have constant circular cross section, are kinematically independent, and have constant mass $m_i \in \mathbb{R}^+$ and variable, but uniform linear density.[1] In addition, PMAs were operated high pressure (high stiffness) and mounted vertically to ensure constant-curvature deformation. Similarly, in application situations involving object manipulation, velocity and payload bounds can be enforced to achieve the same.

B. Recursive Velocities, Jacobians, and Hessians

The kinematics of continuum arms has been well studied over the years [17], [29], [43], [44]. Here, we provide a review of the modal kinematics for multisection continuum arms.

The deformation of a continuum section can be defined by the curve parameters $\lambda(\boldsymbol{q}_i) \in \mathbb{R}^+$ radius of the circular arc, $\phi(\boldsymbol{q}_i) \in \mathbb{R}_0^+$ angle subtended by the circular arc, and $\theta(\boldsymbol{q}_i) \in (-\pi, \pi]$[2] [see Fig. 2(b)]. Employing the curve parameters, the HTM of $\{O_i'\}$ along the neutral axis of the ith continuum section at $\xi_i \in [0,1]$ with respect to $\{O_i\}$, $\mathbf{T}_i : (\boldsymbol{q}_i, \xi_i) \mapsto \mathbb{SE}^3$, is computed as

$$\mathbf{T}_i = \mathbf{R}_Z(\theta_i)\,\mathbf{P}_X(\lambda_i)\,\mathbf{R}_Y(\xi_i\phi_i)\,\mathbf{P}_X(-\lambda_i)\,\mathbf{R}_Z(\theta_i)\cdots$$

$$\mathbf{P}_Z(\sigma_i)\,\mathbf{R}_Z(\gamma_i) = \begin{bmatrix} \mathbf{R}_i & \boldsymbol{p}_i \\ \mathbf{0} & 1 \end{bmatrix} \tag{1}$$

where $\mathbf{P}_X \in \mathbb{SE}^3$, $\mathbf{R}_Z \in \mathbb{SO}^3$, and $\mathbf{R}_Y \in \mathbb{SO}^3$ are HTM that denotes translation along the $+X$-axis, rotation about the $+Z$- and $+Y$-axes, respectively. $\mathbf{R}_i(\boldsymbol{q}_i, \xi_i) \in \mathbb{R}^{3\times 3}$ is the rotation matrix and $\boldsymbol{p}_i(\boldsymbol{q}_i, \xi_i) \in \mathbb{R}^3$ is the position vector. The scalar

[1] These are reasonable assumptions under typical operating conditions without large external forces, as shown in [10] and [36].
[2] As shown in [10], the curve parameters are also functions of unactuated length of PMAs, L_i, and radius of continuum section, r_i, but are not included in the notation (constants for a given continuum arm) for brevity.

ξ_i denotes points along the neutral axis, where $\xi_i = 0$ is the base where $\{O_i'\} \equiv \{O_i\}$ and $\xi_i = 1$ is the tip of the continuum section. We then apply the 13th-order multivariate Taylor series expansion on the terms of (1) to obtain a numerically efficient and stable modal form of the HTM [10].

Employing the continuum section HTM given in (1) and principles of kinematics of serial robot chains, the HTM of any ith section with respect to the task-space coordinate system $\{O\}$, $\mathbf{T}^i : \left(\boldsymbol{q}^i, \xi_i\right) \mapsto \mathbb{SE}^3$, is given by

$$\mathbf{T}^i = \prod_{k=1}^{i} \mathbf{T}_i = \begin{bmatrix} \mathbf{R}^i & \boldsymbol{p}^i \\ \mathbf{0} & 1 \end{bmatrix} \tag{2}$$

where $\mathbf{R}^i\left(\boldsymbol{q}^i, \xi_i\right) \in \mathbb{R}^{3\times 3}$ and $\boldsymbol{p}_i\left(\boldsymbol{q}^i, \xi_i\right) \in \mathbb{R}^3$ define the position and orientation of $\{O_i'\}$ along the neutral axis at ξ_i of the ith continuum section, respectively.

The HTM in (2) can be expanded to obtain the recursive form of the kinematics as

$$\begin{aligned} \mathbf{R}^i &= \mathbf{R}^{i-1}\mathbf{R}_i \\ \boldsymbol{p}^i &= \boldsymbol{p}^{i-1} + \mathbf{R}^{i-1}\boldsymbol{p}_i \end{aligned} \tag{3}$$

where $\mathbf{R}^{i-1}\left(\boldsymbol{q}^{i-1}\right) \in \mathbb{R}^{3\times 3}$ and $\boldsymbol{p}_i\left(\boldsymbol{q}^{i-1}\right) \in \mathbb{R}^3$ are the section tip rotation matrix and the position vector of the preceding continuum section, respectively. Notice the absence of ξ_i as $\xi_k = 1 \forall k < i$, as per the definition of ξ_i [10]. Also, from now on, the dependence variables are not included in the equations for reasons of brevity.

Exploiting the integral Lagrangian formulation [36], we consider a thin disc at ξ_i (which lies on the XY plane of $\{O_i'\}$. Utilizing (3), the angular and linear body velocities with respect to $\{O_i'\}$, $\boldsymbol{\omega}_i\left(\boldsymbol{q}^i, \dot{\boldsymbol{q}}^i\right) \in \mathbb{R}^3$ and $\boldsymbol{v}_i\left(\boldsymbol{q}^i, \dot{\boldsymbol{q}}^i\right) \in \mathbb{R}^3$, respectively, can be defined as

$$\begin{aligned} \boldsymbol{\Omega}_i &= \mathbf{R}_i^T\left(\boldsymbol{\Omega}_{i-1}\mathbf{R}_i + \dot{\mathbf{R}}_i\right) \\ \boldsymbol{v}_i &= \mathbf{R}_i^T\left(\boldsymbol{v}_{i-1} + \boldsymbol{\Omega}_{i-1}\boldsymbol{p}_i + \dot{\boldsymbol{p}}_i\right) \end{aligned} \tag{4}$$

where we define $\boldsymbol{\Omega}_i\left(\boldsymbol{q}^i, \dot{\boldsymbol{q}}^i\right) \in \mathbb{R}^{3\times 3}$ and $\boldsymbol{\omega}_i = \boldsymbol{\Omega}_i^{\vee}$ for ease of subsequent development of the EoM. The derivations are outlined in Appendixes A and B.

As shown in [36], Jacobians and Hessians play a critical role in recursive development of the EoM. Applying the standard techniques, the angular and linear velocity Jacobians, $\mathbf{J}_i^{\omega}\left(\boldsymbol{q}^i, \xi_i\right) \in \mathbb{R}^{3\times 3n}$ and $\mathbf{J}_i^{v}\left(\boldsymbol{q}^i, \xi_i\right) \in \mathbb{R}^{3\times 3n}$, respectively, are derived. We use the property $\boldsymbol{\omega}_i = \boldsymbol{\Omega}_i^{\vee}$ to define $\mathbf{J}_i^{\Omega}\left(\boldsymbol{q}^i, \xi_i\right) \in \mathbb{R}^{3\times 9n}$, in the development of the EoM, and it is given by

$$\mathbf{J}_i^{\Omega} = \mathbf{R}_i^T\left[\mathbf{J}_{i-1}^{\Omega}\mathbf{R}_i \middle| \mathbf{R}_{i,\boldsymbol{q}_i}\right] \tag{5}$$

where $\mathbf{J}_i^{\omega} = \left(\mathbf{J}_i^{\Omega}\right)^{\vee}$ and $\mathbf{J}_{i-1}^{\Omega}\left(\boldsymbol{q}^{i-1}\right) \in \mathbb{R}^{3\times 9(n-1)}$. Appendix C details the derivation.

Taking the partial derivative of (5) with respect to $\boldsymbol{q}^i$, the angular body velocity Hessian, $\mathbf{H}_i^{\Omega} = \mathbf{J}_{i,\boldsymbol{q}_i}^{\Omega}\left(\boldsymbol{q}^i, \xi_i\right) \in \mathbb{R}^{9n\times 9n}$, is given by

$$\mathbf{H}_i^{\Omega} = \left[\begin{array}{c|c} \mathbf{R}_i^T\mathbf{H}_{i-1}^{\Omega}\mathbf{R}_i & \mathbf{0} \\ \hline \mathbf{R}_{i,\boldsymbol{q}_i}^T\mathbf{J}_{i-1}^{\Omega}\mathbf{R}_i\cdots & \mathbf{R}_{i,\boldsymbol{q}_i}^T\mathbf{R}_{i,\boldsymbol{q}_i^T}\cdots \\ \quad +\mathbf{R}_i^T\mathbf{J}_{i-1}^{\Omega}\mathbf{R}_{i,\boldsymbol{q}_i} & \quad +\mathbf{R}_i^T\mathbf{R}_{i,\boldsymbol{q}_i^T,\boldsymbol{q}_i} \end{array}\right] \tag{6}$$

where $\mathbf{H}_{i-1}^{\Omega}\left(\boldsymbol{q}^{i-1}\right) \in \mathbb{R}^{9(n-1)\times 9(n-1)}$. Refer to Appendix E for the derivation.

Similarly, the linear velocity Jacobian, $\mathbf{J}_i^{v}$, and Hessian, $\mathbf{H}_i^{v} = \mathbf{J}_{i,\boldsymbol{q}_i}^{v}\left(\boldsymbol{q}^i, \xi_i\right) \in \mathbb{R}^{9n\times 3n}$, are given by

$$\mathbf{J}_i^{v} = \mathbf{R}_i^T\left[\mathbf{J}_{i-1}^{v} + \mathbf{J}_{i-1}^{\Omega}\boldsymbol{p}_i \middle| \boldsymbol{p}_{i,\boldsymbol{q}_i^T}\right] \tag{7}$$

$$\mathbf{H}_i^{v} = \left[\begin{array}{c|c} \mathbf{R}_i^T\left(\mathbf{H}_{i-1}^{v} + \mathbf{H}_{i-1}^{\Omega}\boldsymbol{p}_i\right) & \mathbf{0} \\ \hline \mathbf{R}_{i,\boldsymbol{q}_i}^T\left(\mathbf{J}_{i-1}^{v} + \mathbf{J}_{i-1}^{\Omega}\boldsymbol{p}_i\right)\cdots & \mathbf{R}_{i,\boldsymbol{q}_i}^T\boldsymbol{p}_{i,\boldsymbol{q}_i^T}\cdots \\ \quad +\mathbf{R}_i^T\mathbf{J}_{i-1}^{\Omega}\boldsymbol{p}_{i,\boldsymbol{q}_i} & \quad +\mathbf{R}_i^T\boldsymbol{p}_{i,\boldsymbol{q}_i^T,\boldsymbol{q}_i} \end{array}\right] \tag{8}$$

where $\mathbf{J}_{i-1}^{v}(\boldsymbol{q}^{i-1}, \xi_i) \in \mathbb{R}^{3\times 3(n-1)}$, $\mathbf{H}_{i-1}^{v}(\boldsymbol{q}^{i-1}) \in \mathbb{R}^{9(n-1)\times 3(n-1)}$, and the derivation is listed in Appendixes D and F.

C. Extension for Kinematics of Centers of Gravity

Similar to Section II-B, without losing generality, we derive the kinematics for the CoG of any ith section. We define a coordinate system at the CoG, $\left\{\overline{O}_i\right\}$, whose HTM, $\overline{\mathbf{T}}_i : (\boldsymbol{q}_i) \mapsto \mathbb{SE}^3$, with respect to $\{O_i\}$ is defined as

$$\overline{\mathbf{T}}_i = \int \mathbf{T}_i = \begin{bmatrix} \overline{\mathbf{R}}_i & \overline{\boldsymbol{p}}_i \\ \mathbf{0} & 1 \end{bmatrix} \tag{9}$$

where $\overline{\mathbf{R}}_i = \int \mathbf{R}_i\left(\boldsymbol{q}_i\right) \in \mathbb{R}^{3\times 3}$ is the resultant rotation matrix and $\overline{\boldsymbol{p}}_i = \int \boldsymbol{p}_i\left(\boldsymbol{q}_i\right) \in \mathbb{R}^3$ is the position vector [40]. Note that the CoG is a function of $\boldsymbol{q}_i$ and, therefore, varies as the continuum section deforms.

To derive the kinematics of the CoG coordinate frame, $\left\{\overline{O}_i\right\}$, with respect to $\{O\}$, we can combine $\overline{\mathbf{T}}_i$ with the general HTM given in (2). From the definition, $\left\{O_{i-1}'|_{\xi_{i-1}=1}\right\} \equiv \{O_i\}$ [see Fig. 2(b)], and therefore, CoG of the ith section relative to $\{O\}$, $\overline{\mathbf{T}}^i : \left(\boldsymbol{q}^i\right) \mapsto \mathbb{SE}^3$, can be defined as

$$\overline{\mathbf{T}}^i = \int \mathbf{T}^{i-1}\mathbf{T}_i = \left(\prod_{k=1}^{i-1}\mathbf{T}_k\right)\left(\int \mathbf{T}_i\right) = \begin{bmatrix} \overline{\mathbf{R}}^i & \overline{\boldsymbol{p}}^i \\ \mathbf{0} & 1 \end{bmatrix} \tag{10}$$

where $\overline{\mathbf{R}}^i\left(\boldsymbol{q}^i\right) \in \mathbb{R}^{3\times 3}$ is orientation and $\overline{\boldsymbol{p}}_i\left(\boldsymbol{q}^i\right) \in \mathbb{R}^3$ are position matrices of the CoG coordinate frame.

Akin to (3), the recursive forms of $\overline{\mathbf{R}}^i$ and $\overline{\boldsymbol{p}}^i$ are given by

$$\begin{aligned} \overline{\mathbf{R}}^i &= \mathbf{R}^{i-1}\overline{\mathbf{R}}_i \\ \overline{\boldsymbol{p}}^i &= \boldsymbol{p}^{i-1} + \mathbf{R}^{i-1}\overline{\boldsymbol{p}}_i \end{aligned} \tag{11}$$

where $\mathbf{R}^{i-1}$ and $\boldsymbol{p}^{i-1}$ are formulated from (3).

Similar to (4), the angular and linear body velocities of the CoG (relative to $\left\{\overline{O}_i\right\}$), $\overline{\boldsymbol{\omega}}_i\left(\boldsymbol{q}^i, \dot{\boldsymbol{q}}^i\right) \in \mathbb{R}^3$ and $\overline{\boldsymbol{v}}_i\left(\boldsymbol{q}^i, \dot{\boldsymbol{q}}^i\right) \in \mathbb{R}^3$ can be derived as

$$\begin{aligned} \overline{\boldsymbol{\Omega}}_i &= \overline{\mathbf{R}}_i^T\left(\boldsymbol{\Omega}_{i-1}\overline{\mathbf{R}}_i + \dot{\overline{\mathbf{R}}}_i\right) \\ \overline{\boldsymbol{v}}_i &= \overline{\mathbf{R}}_i^T\left(\boldsymbol{v}_{i-1} + \boldsymbol{\Omega}_{i-1}\overline{\boldsymbol{p}}_i + \dot{\overline{\boldsymbol{p}}}_i\right) \end{aligned} \tag{12}$$

where $\boldsymbol{v}_{i-1}$ and $\boldsymbol{\Omega}_{i-1}$, defined in (4), are linear and angular velocities at the tip of the $(i-1)$ th continuum section, respectively. Here too, we employ the relationship $\overline{\boldsymbol{\omega}}_i = \overline{\boldsymbol{\Omega}}_i^{\vee}$ to compute $\overline{\boldsymbol{\Omega}}_i\left(\boldsymbol{q}^i, \dot{\boldsymbol{q}}^i\right) \in \mathbb{R}^{3\times 3}$.

Analogous to (5)–(8), the angular body velocity Jacobian of CoG, $\overline{\mathbf{J}}_i^{\Omega}\left(\boldsymbol{q}^i\right) \in \mathbb{R}^{3\times 9n}$, Hessian $\overline{\mathbf{H}}_i^{\Omega}\left(\boldsymbol{q}^i\right) \in \mathbb{R}^{9n\times 9n}$, linear body velocity Jacobian, $\overline{\mathbf{J}}_i^{v}\left(\boldsymbol{q}^i\right) \in \mathbb{R}^{3\times 3n}$, and Hessian $\overline{\mathbf{H}}_i^{v}\left(\boldsymbol{q}^i\right) \in \mathbb{R}^{9n\times 3n}$, are, respectively, given by (13)–(16) as

$$\overline{\mathbf{J}}_i^{\Omega} = \overline{\mathbf{R}}_i^T\left[\mathbf{J}_{i-1}^{\Omega}\overline{\mathbf{R}}_i \middle| \overline{\mathbf{R}}_{i,\boldsymbol{q}_i^T}\right] \tag{13}$$

$$\overline{\mathbf{H}}_i^{\Omega} = \left[\begin{array}{c|c} \overline{\mathbf{R}}_i^T\mathbf{H}_{i-1}^{\Omega}\overline{\mathbf{R}}_i & \mathbf{0} \\ \hline \overline{\mathbf{R}}_{i,\boldsymbol{q}_i}^T\mathbf{J}_{i-1}^{\Omega}\overline{\mathbf{R}}_i\cdots & \overline{\mathbf{R}}_{i,\boldsymbol{q}_i}^T\overline{\mathbf{R}}_{i,\boldsymbol{q}_i^T}\cdots \\ +\overline{\mathbf{R}}_i^T\mathbf{J}_{i-1}^{\Omega}\overline{\mathbf{R}}_{i,\boldsymbol{q}_i} & +\overline{\mathbf{R}}_i^T\overline{\mathbf{R}}_{i,\boldsymbol{q}_i^T,\boldsymbol{q}_i} \end{array}\right] \tag{14}$$

$$\overline{\mathbf{J}}_i^{v} = \overline{\mathbf{R}}_i^T\left[\mathbf{J}_{i-1}^{v} + \mathbf{J}_{i-1}^{\Omega}\overline{\boldsymbol{p}}_i \middle| \overline{\boldsymbol{p}}_{i,\boldsymbol{q}_i^T}\right] \tag{15}$$

$$\overline{\mathbf{H}}_i^{v} = \left[\begin{array}{c|c} \overline{\mathbf{R}}_i^T\left(\mathbf{H}_{i-1}^{v} + \mathbf{H}_{i-1}^{\Omega}\overline{\boldsymbol{p}}_i\right) & \mathbf{0} \\ \hline \overline{\mathbf{R}}_{i,\boldsymbol{q}_i}^T\left(\mathbf{J}_{i-1}^{v} + \mathbf{J}_{i-1}^{\Omega}\overline{\boldsymbol{p}}_i\right)\cdots & \overline{\mathbf{R}}_{i,\boldsymbol{q}_i}^T\overline{\boldsymbol{p}}_{i,\boldsymbol{q}_i^T}\cdots \\ +\overline{\mathbf{R}}_i^T\mathbf{J}_{i-1}^{\Omega}\overline{\boldsymbol{p}}_{i,\boldsymbol{q}_i} & +\overline{\mathbf{R}}_i^T\overline{\boldsymbol{p}}_{i,\boldsymbol{q}_i^T,\boldsymbol{q}_i} \end{array}\right]. \tag{16}$$

D. Case Study: Point Versus Nonpoint Mass at the CoG

Consider the CoG velocities depicted in (12) when $\boldsymbol{\Omega}_{i-1} = [0, 0, \omega_z]$ with $\omega_z \neq 0$, $\boldsymbol{v}_{i-1} = 0$, $\boldsymbol{q}_i = 0$, and $\dot{\boldsymbol{q}}_i = 0$. Physically, this refers to a nonactuating ith continuum section (essentially a cylinder of length L_{i0} and radius r_i, whose CoG is located at the midpoint, i.e., $\overline{\boldsymbol{p}}_i = \left[0, 0, \frac{L_{i0}}{2}\right]$, of the neutral axis, where the tip of the $(i-1)$ th section rotates in place without translation. This scenario is theoretically possible and demonstrated in [10], where kinematic decoupling is present in multisection continuum arms. From (12), the CoG velocities become $\overline{\boldsymbol{\Omega}}_i = \boldsymbol{\Omega}_{i-1}$ and $\overline{\boldsymbol{v}}_i = 0$. The kinetic energies of the ith section then become $\mathcal{K}_i^{\omega} = \frac{1}{4}m_i r_i^2\omega_z^2$ and $\mathcal{K}_i^{v} = 0$. If a point mass is considered at the CoG, it will result in $\overline{\mathcal{K}}_i^{\omega} = \overline{\mathcal{K}}_i^{v} = 0$. As a result, a point-mass model is inadequate for modeling multisection continuum arms. Thus, in this paper, we will consider a hypothetical thin disc of mass m_i and radius r_i on the XY plane of $\left\{\overline{O}_i\right\}$ with its geometric center coinciding the origin of $\left\{\overline{O}_i\right\}$, i.e., at the CoG [see Fig. 2(b)]. The kinetic energies then become $\overline{\mathcal{K}}_i^{\omega} = \frac{1}{4}m_i r_i^2\omega_z^2$ and $\overline{\mathcal{K}}_i^{v} = 0$ to match that of the actual continuum section energy. Employing the disc model at the CoG, Section III derives the energy-shaping coefficients [40] to match energies to that of the integral model reported in [36].

III. Derive Energy Balance of the CoG-Based System

A. Continuum Section Kinetic Energy: Integral and CoG-Based Models

Without losing generality, we next derive the kinetic energies, angular and linear, for any ith continuum section. Then, we compare the terms to formulate the energy scaling conditions. Analogous to [36], to find the kinetic energy of the continuum section using an integral approach, we will consider an infinitesimally thin disc of radius r_i along the length of the continuum section. By applying the body velocities given by (4), the energy computed for a disc is then integrated with respect to ξ_i to compute the section energy. The angular kinetic energy, $\mathcal{K}_i^{\omega} : \left(\boldsymbol{q}^i, \dot{\boldsymbol{q}}^i\right) \mapsto \mathbb{R}_0^+$, is given by

$$\begin{aligned}\mathcal{K}_i^{\omega} &= \int\left(\frac{1}{2}\boldsymbol{\omega}_i^T\mathcal{M}_i^{\omega}\boldsymbol{\omega}_i\right) = \frac{1}{2}I_{xx}\mathbb{T}_2\left(\int\boldsymbol{\Omega}_i^T\boldsymbol{\Omega}_i\right)\\ &= \frac{1}{2}I_{xx}\mathbb{T}_2\left(\int\mathbf{R}_i^T\boldsymbol{\Omega}_{i-1}^T\boldsymbol{\Omega}_{i-1}\mathbf{R}_i\cdots\right.\\ &\qquad \left.+2\int\dot{\mathbf{R}}_i^T\boldsymbol{\Omega}_{i-1}\mathbf{R}_i + \int\dot{\mathbf{R}}_i^T\dot{\mathbf{R}}_i\right)\end{aligned} \tag{17}$$

where $I_{xx} = \frac{1}{4}m_i r_i^2$ is the moment of inertia about the X-axis of $\{O_i'\}$.

Using the angular velocity given in (12), the angular kinetic energy of the disc at the CoG, $\overline{\mathcal{K}}_i^{\omega} : \left(\boldsymbol{q}^i, \dot{\boldsymbol{q}}^i\right) \mapsto \mathbb{R}_0^+$, becomes

$$\begin{aligned}\overline{\mathcal{K}}_i^{\omega} &= \frac{1}{2}\overline{\boldsymbol{\omega}}_i^T\mathcal{M}_i^{\omega}\overline{\boldsymbol{\omega}}_i = \frac{1}{2}I_{xx}\mathbb{T}_2\left(\overline{\boldsymbol{\Omega}}_i^T\overline{\boldsymbol{\Omega}}_i\right)\\ &= \frac{1}{2}I_{xx}\mathbb{T}_2\left(\overline{\mathbf{R}}_i^T\boldsymbol{\Omega}_{i-1}^T\boldsymbol{\Omega}_{i-1}\overline{\mathbf{R}}_i + 2\dot{\overline{\mathbf{R}}}_i^T\boldsymbol{\Omega}_{i-1}\overline{\mathbf{R}}_i + \dot{\overline{\mathbf{R}}}_i^T\dot{\overline{\mathbf{R}}}_i\right)\end{aligned} \tag{18}$$

Similarly, using the linear body velocity in (4), the linear kinetic energy of the continuous model, $\mathcal{K}_i^{v} : \left(\boldsymbol{q}^i, \dot{\boldsymbol{q}}^i\right) \mapsto \mathbb{R}_0^+$, can be computed as

$$\begin{aligned}\mathcal{K}_i^{v} &= \int\left(\frac{1}{2}\boldsymbol{v}_i^T\mathcal{M}_i^{v}\boldsymbol{v}_i\right)\\ &= \frac{1}{2}m_i\left(\boldsymbol{v}_{i-1}^T\boldsymbol{v}_{i-1} + 2\boldsymbol{v}_{i-1}^T\boldsymbol{\Omega}_{i-1}\overline{\boldsymbol{p}}_i + 2\boldsymbol{v}_{i-1}^T\dot{\overline{\boldsymbol{p}}}_i\cdots\right.\\ &\qquad \left.+\int\boldsymbol{p}_i^T\boldsymbol{\Omega}_{i-1}^T\boldsymbol{\Omega}_{i-1}\boldsymbol{p}_i + 2\int\boldsymbol{p}_i^T\boldsymbol{\Omega}_{i-1}^T\dot{\boldsymbol{p}}_i + \int\dot{\boldsymbol{p}}_i^T\dot{\boldsymbol{p}}_i\right)\end{aligned} \tag{19}$$

where $\mathcal{M}_i^{v} = m_i\mathbf{I}_3$. Additionally, the CoG model's linear kinetic energy, $\overline{\mathcal{K}}_i^{v} : \left(\boldsymbol{q}^i, \dot{\boldsymbol{q}}^i\right) \mapsto \mathbb{R}_0^+$, is derived as

$$\begin{aligned}\overline{\mathcal{K}}_i^{v} &= \frac{1}{2}\overline{\boldsymbol{v}}_i^T\mathcal{M}_i^{v}\overline{\boldsymbol{v}}_i = \frac{1}{2}m_i\left(\boldsymbol{v}_{i-1}^T\boldsymbol{v}_{i-1} + 2\boldsymbol{v}_{i-1}^T\boldsymbol{\Omega}_{i-1}\overline{\boldsymbol{p}}_i\cdots\right.\\ &\qquad \left.+2\boldsymbol{v}_{i-1}^T\dot{\overline{\boldsymbol{p}}}_i + \overline{\boldsymbol{p}}_i^T\boldsymbol{\Omega}_{i-1}^T\boldsymbol{\Omega}_{i-1}\overline{\boldsymbol{p}}_i + 2\overline{\boldsymbol{p}}_i^T\boldsymbol{\Omega}_{i-1}^T\dot{\overline{\boldsymbol{p}}}_i + \dot{\overline{\boldsymbol{p}}}_i^T\dot{\overline{\boldsymbol{p}}}_i\right).\end{aligned} \tag{20}$$

B. Minimize Energy Difference Between the Integral and CoG-Based Models

In this section, utilizing the energies derived in Section III-A, we systematically derive scalars to match the kinetic energy of the CoG models to that of the integral model. Unlike the single-section case [40] however, the kinetic energy is dependent on the velocities of the ith section, as well as the previous sections. Consider the angular energy difference between the models, derived for the ith continuum section, given by

$$\begin{aligned}\mathcal{K}_i^{\omega} - \overline{\mathcal{K}}_i^{\omega} &= \frac{1}{2}I_{xx}\mathbb{T}_2\left(\int\dot{\mathbf{R}}_i^T\dot{\mathbf{R}}_i - \beta_3^{\omega}\dot{\overline{\mathbf{R}}}_i^T\dot{\overline{\mathbf{R}}}_i\cdots\right.\\ &\quad +2\int\mathbf{R}_i^T\boldsymbol{\Omega}_{i-1}^T\boldsymbol{\Omega}_{i-1}\mathbf{R}_i - 2\beta_1^{\omega}\overline{\mathbf{R}}_i^T\boldsymbol{\Omega}_{i-1}^T\boldsymbol{\Omega}_{i-1}\overline{\mathbf{R}}_i\cdots\\ &\quad \left.+\int\dot{\mathbf{R}}_i^T\boldsymbol{\Omega}_{i-1}\mathbf{R}_i - \beta_2^{\omega}\dot{\overline{\mathbf{R}}}_i^T\boldsymbol{\Omega}_{i-1}\overline{\mathbf{R}}_i\right)\end{aligned} \tag{21}$$

where $\beta_k^{\omega}\ \forall k \in \{1,2,3\}$ are the energy-shaping coefficients that we apply to the CoG energy terms to match the energies.

Note that, in this case, unlike the single-section case reported in [41], we have three terms that do not get canceled when taking the difference. Likewise, the linear kinetic energy difference is computed as

$$\mathcal{K}_i^{\upsilon} - \overline{\mathcal{K}}_i^{\upsilon} = \frac{1}{2} m_i \left(\int \boldsymbol{p}_i^T \boldsymbol{\Omega}_{i-1}^T \boldsymbol{\Omega}_{i-1} \boldsymbol{p}_i - \beta_1^{\upsilon} \overline{\boldsymbol{p}}_i^T \boldsymbol{\Omega}_{i-1}^T \boldsymbol{\Omega}_{i-1} \overline{\boldsymbol{p}}_i \cdots \right.$$
$$+ 2 \int \boldsymbol{p}_i^T \boldsymbol{\Omega}_{i-1}^T \dot{\boldsymbol{p}}_i - 2\beta_2^{\upsilon} \overline{\boldsymbol{p}}_i^T \boldsymbol{\Omega}_{i-1}^T \dot{\overline{\boldsymbol{p}}}_i \cdots$$
$$\left. + \int \dot{\boldsymbol{p}}_i^T \dot{\boldsymbol{p}}_i - \beta_3^{\upsilon} \dot{\overline{\boldsymbol{p}}}_i^T \dot{\overline{\boldsymbol{p}}}_i \right). \tag{22}$$

Notice that some terms are canceled due to the absence of products of integrable terms, thus resulting in three remaining terms. We introduce the energy-shaping coefficients, $\beta_k^{\upsilon}\ \forall k \in \{1,2,3\}$, for each of those terms. The coefficients, introduced in (21) and (22), will be solved in the latter part of this section through a multivariate optimization routine.

1) Generate Random Sample Set: Including the physical robot parameters such as L_{i0}, l_i, and r_i, the energy differences given by (21) and (22) become functions of $(\alpha_l, \alpha_r, \boldsymbol{q}_i, \dot{\boldsymbol{q}}_i, \boldsymbol{\Omega}_{i-1}) \in \mathbb{R}^{11}$, where $\alpha_l = \frac{\max(l_i)}{L_{i0}}$ and $\alpha_r = \frac{r_i}{L_{i0}}$ are the normalized length and radius of the continuum section. Similarly, we generate 10^7 random combinations of $\alpha_r \in \left[\frac{1}{20}, \frac{1}{2}\right]$, $\alpha_l \in \left[\frac{1}{20}, 6\pi\alpha_r\right]$, $\boldsymbol{q}_i \in [0, \alpha_l L_{i0}]$, and $\dot{\boldsymbol{q}}_i \in [0, L_{i0}]$. The upper bound of α_l limits the maximum bending angle of continuum sections to $\frac{4\pi}{3}$. Also, note that $\boldsymbol{\Omega}_{i-1}$ depends on $\left(\boldsymbol{q}^{i-1}, \dot{\boldsymbol{q}}^{i-1}\right)$, and for a general ith section, it is not possible to sample the joint-space variables since i is arbitrary. To overcome this challenge, we generate random $\boldsymbol{\Omega}_{i-1}$, where each component is chosen from the range $\left[-10^2, 10^2\right]$. Note that these parametric bounds for $\boldsymbol{\Omega}_{i-1}$ and α_l, though arbitrary and unrealistically large for physical continuum arms, were chosen to ensure the rigor and generality of the proposed model and within the error bounds of the 13th-order modal shape functions used in this paper. However, one may increase this bound (which would also require adjusting the order of modal shape functions of the HTM elements to meet the desired position and orientation error metrics at the tip at the maximum bending). More details related to choosing expansion order and errors can be found in [10].

2) Computing the Energy-Shaping Coefficients: For the random combinations of joint-space variables and physical parameters generated in the previous step, corresponding kinetic energy differences of the integral and CoG-based models, depicted in (21) and (22), are computed. As suggested by the definitions, for the ease of comparison of corresponding terms, we computed the three residual terms of each of kinetic energy differences separately. For instance, in the case of $\mathcal{K}_i^{\omega}$, terms $\mathbb{T}_2(\int \mathbf{R}_i^T \boldsymbol{\Omega}_{i-1}^T \boldsymbol{\Omega}_{i-1} \mathbf{R}_i)$, $2\mathbb{T}_2(\int \dot{\mathbf{R}}_i^T \boldsymbol{\Omega}_{i-1} \mathbf{R}_i)$, and $\mathbb{T}_2(\int \dot{\mathbf{R}}_i^T \dot{\mathbf{R}}_i)$ are computed separately. Similarly, for $\overline{\mathcal{K}}_i^{\omega}$, $\mathbb{T}_2(\overline{\mathbf{R}}_i^T \boldsymbol{\Omega}_{i-1}^T \boldsymbol{\Omega}_{i-1} \overline{\mathbf{R}}_i)$, $2\mathbb{T}_2(\dot{\overline{\mathbf{R}}}_i^T \boldsymbol{\Omega}_{i-1} \overline{\mathbf{R}}_i)$, and $\mathbb{T}_2(\dot{\overline{\mathbf{R}}}_i^T \dot{\overline{\mathbf{R}}}_i)$ are computed separately. Then, the sum of these terms, scaled by $\frac{1}{2} I_{xx}$, will yield the energy difference, $\mathcal{K}_i^{\omega} - \overline{\mathcal{K}}_i^{\omega}$. The same approach is followed for the linear kinetic energy difference given by (22) and scaled by $\frac{m_i}{2}$. The corresponding terms for the integral system and the CoG-based system are then plotted against each other in Fig. 3.

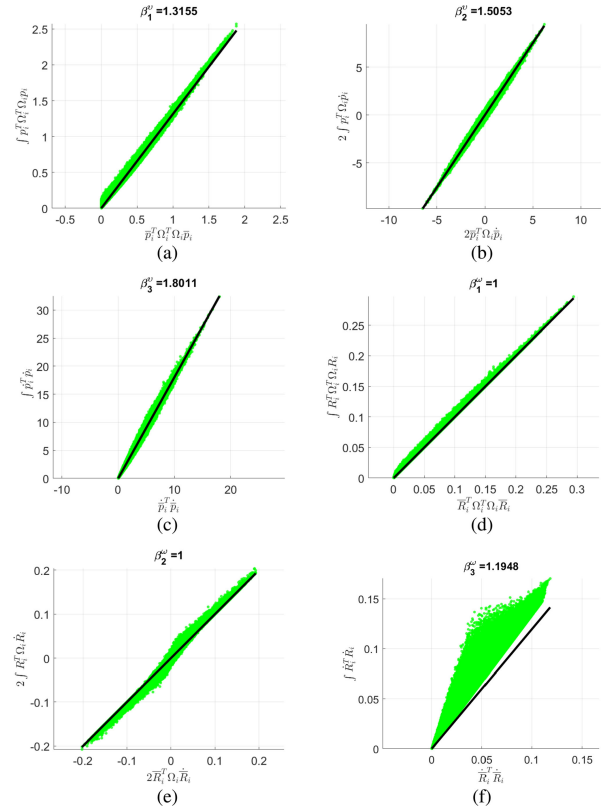

Fig. 3. Comparison of the ratios of energy terms given by (22): (a) $\int \boldsymbol{p}_i^T \boldsymbol{\Omega}_{i-1}^T \boldsymbol{\Omega}_{i-1} \boldsymbol{p}_i$ versus $\overline{\boldsymbol{p}}_i^T \boldsymbol{\Omega}_{i-1}^T \boldsymbol{\Omega}_{i-1} \overline{\boldsymbol{p}}_i$, $R^2 = 0.998$ (where R^2 is the coefficient of determination, also known as R-squared), (b) $\int \boldsymbol{p}_i^T \boldsymbol{\Omega}_{i-1}^T \dot{\boldsymbol{p}}_i$ versus $\overline{\boldsymbol{p}}_i^T \boldsymbol{\Omega}_{i-1}^T \dot{\overline{\boldsymbol{p}}}_i$, $R^2 = 0.9966$, and (c) $\int \dot{\boldsymbol{p}}_i^T \dot{\boldsymbol{p}}_i$ versus $\dot{\overline{\boldsymbol{p}}}_i^T \dot{\overline{\boldsymbol{p}}}_i R^2 = 0.9984$. Similarly, the comparison of the ratio of energy terms given by (21): (d) $\int \dot{\mathbf{R}}_i^T \dot{\mathbf{R}}_i$ versus $\dot{\overline{\mathbf{R}}}_i^T \dot{\overline{\mathbf{R}}}_i$, $R^2 = 0.9993$, (e) $2\int \mathbf{R}_i^T \boldsymbol{\Omega}_{i-1}^T \boldsymbol{\Omega}_{i-1} \mathbf{R}_i$ versus $2\overline{\mathbf{R}}_i^T \boldsymbol{\Omega}_{i-1}^T \boldsymbol{\Omega}_{i-1} \overline{\mathbf{R}}_i$, $R^2 = 0.9975$, and (f) $\int \dot{\mathbf{R}}_i^T \boldsymbol{\Omega}_{i-1} \mathbf{R}_i$ versus $\dot{\overline{\mathbf{R}}}_i^T \boldsymbol{\Omega}_{i-1} \overline{\mathbf{R}}_i$, $R^2 = 0.9914$. The strong correlation between the terms are evidenced by less than 5×10^{-4} (<0.036% normalized to coefficients) 95% confidence intervals for each fit.

It can be seen that, despite the variation of the physical shape ($\max(l_{ij})$ and r_i), there are proportional relationships between the matching terms of the two analytical models. This indicates us that the fundamental variable-length continuum section behavior across the two systems is proportional and independent of the physical shape. The proportional constants can be computed in two ways. One approach is to consider matching terms individually and compute the least-squares linear fit. The other approach is to consider the kinetic energy of the entire system and find the optimal coefficients that would minimize the cumulative energy difference. In this paper, we have opted for the latter approach, since it provided a slight, though negligible, improvement in energy matching. We formulated our optimization problem in MATLAB 2017a and used global optimization on the in-built fmincon multivariate constrained optimization subroutine using the objective function $\mathcal{K}_i^{\upsilon} - \overline{\mathcal{K}}_i^{\upsilon}(\beta^{\upsilon}) +$

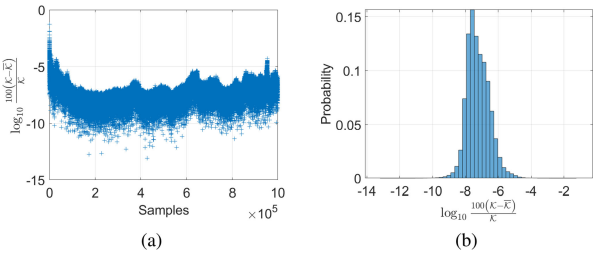

Fig. 4. Normalized energy difference between the integral and CoG-based modeling approaches for a ten-section continuum arm. (a) Energy difference for 10^6 randomly selected joint-space displacement and velocity samples. (b) Histogram of the normalized energy difference for the same samples.

$\mathcal{K}_i^{\omega} - \overline{\mathcal{K}}_i^{\omega}\,(\beta^{\omega})$ for all 10^7 parametric combinations. Noting the direct proportionality, we bounded the scalar range to $[0, 1]$ for numerical efficiency. The resultant energy-shaping coefficient values are shown in Fig. 3.

Notice that the proportional coefficient of Fig. 3(f) is slightly more aggressive than what the data suggest. The reason is the difference of the ratio of contributions from individual terms. For instance, the contribution of the term $\frac{m_i}{2}\int \dot{\boldsymbol{p}}_i^T \dot{\boldsymbol{p}}_i$ is orders of magnitude greater than that of the term $\frac{1}{2} I_{xx} \mathbb{T}_2 (\int \dot{\mathbf{R}}_i^T \dot{\mathbf{R}}_i)$. The system-wide energy consideration would then place more emphasis on larger contributors to yield optimal energy scalars, and this explains the suboptimal results of the termwise computation of proportional coefficients. However, based on our computations, given the strong correlation of the energy terms ($< \pm 0.036\%$ normalized 95% bound) between the two modeling approaches, either method produces sufficient accuracy for practical purposes.

3) Numerical Validation of Energy-Shaping Coefficients: In this section, we statistically validate the coefficients generated in the previous section for a ten-section continuum robot model. For an n-section continuum arm, $6n$ variables are required to compute the kinetic energy ($3n$ joint-space displacements and velocities each). Assuming $L_0 = 0.15\,\text{m}$, $r_i = 0.0125\,\text{m}$, and $m_i = 0.1\,\text{kg}$ [physical parameters corresponding to the prototype arm shown in Fig. 1(a)], here, we generate 10^6 random sample values based on uniform distribution (to ensure accurate statistical distribution of error) within $[0, 0.07\,\text{m}]$ and $[-L_0, L_0]\,\text{ms}^{-1}$ for $\boldsymbol{q}$ and $\dot{\boldsymbol{q}}$, respectively, for the continuum arm numerical model. The difference of the complete system kinetic energies is computed by taking the cumulative of sectionwise energy differences given by (21) and (22). The energy difference percentages, normalized to max $(\mathcal{K}_i^{v} + \mathcal{K}_i^{\omega})$, for each sample, are then computed and plotted in Fig. 4(a). Note that $\max(\mathcal{K}_i^{v} + \mathcal{K}_i^{\omega})$ is not the absolute maximum kinetic energy for the given robot, but rather it is a statistical upper bound, and therefore, the energy percentage errors computed here are conservative, and the actual error is likely to be significantly lower in practice. The percentage error distribution is shown in Fig. 4(b). The figure shows that the energy difference is essentially negligible with less than 10^{-7} mean percentage error. The results show that the computed energy scalars are accurate and applicable for arbitrary length continuum arms without undesirable error propagation, eliminating the need for complex integral terms.

C. Potential Energy of Continuum Sections

As reported in [36], a continuum arm is subjected to gravitational and elastic potential energies. Elastic potential energy, given by $\mathcal{P}^e = \frac{1}{2}\boldsymbol{q}^T \mathbf{K}_e \boldsymbol{q}$, only depends on $\boldsymbol{q}$ and is, therefore, independent of the modeling approach herein. The gravitational potential energy for the integral and CoG-based model can be defined as $\mathcal{P}_i^g = \int m_i \boldsymbol{g}^T \boldsymbol{p}^i$ and $\overline{\mathcal{P}}_i^g = m_i \boldsymbol{g}^T \overline{\boldsymbol{p}}^i$, respectively. Note that $\mathcal{P}_i^g$ does not contain products of integrable terms. Therefore, $\mathcal{P}_i^g$ can be simplified to $\mathcal{P}_i^g = m_i \boldsymbol{g}^T \left(\int \boldsymbol{p}^i\right)$ and, from the definition (10), then becomes $\mathcal{P}_i^g = m_i \boldsymbol{g}^T \left(\overline{\boldsymbol{p}}^i\right) = \overline{\mathcal{P}}_i^g$. Thus, the gravitational potential energy is identical in both models.

IV. Recursive Formulation of EoMs

This section utilizes the energy relationships derived in Section III-B2 to formulate the recursive form of the EoM. Let the Lagrangian of the system using the CoG-based model be $\overline{\mathcal{K}} - \overline{\mathcal{P}}$. Then, the EoM in standard form is given by

$$\overline{\mathbf{M}}\ddot{\boldsymbol{q}} + \overline{\mathbf{C}}\dot{\boldsymbol{q}} + \overline{\boldsymbol{G}} = \boldsymbol{\tau} \tag{23}$$

where $\overline{\mathbf{M}} \in \mathbb{R}^{3n \times 3n}$, $\overline{\mathbf{C}} \in \mathbb{R}^{3n \times 3n}$, $\overline{\boldsymbol{G}} \in \mathbb{R}^{3n \times 1}$, and $\tau \in \mathbb{R}^{3n \times 1}$ are generalized inertia matrix, centrifugal and Coriolis force matrix, conservative force matrix, and joint-space input force vector, respectively.

From the theorems derived in [36], we can decompose these matrices into sectionwise contributions as $\overline{\mathbf{M}} = \sum \overline{\mathbf{M}}_i$, $\overline{\mathbf{C}} = \sum \overline{\mathbf{C}}_i$, and $\overline{\boldsymbol{G}} = \sum \overline{\boldsymbol{G}}_i$, respectively. In this section, we derive the sectionwise contributions in recursive form to compute the EoM in (23). Note that the CoG-based model was derived by integrating the integral terms with respect to ξ, a scalar (see Section II-C). As a result, the joint-space terms between the integral Lagrangian and CoG-based models remain unaffected during EoM formulation via Lagrangian principles.

A. Generalized Inertia Matrix $\left(\overline{\mathbf{M}}_i\right)$

Analogous to the integral modeling approach [36], we can define the ith section kinetic energy to be the sum of the scaled (using the energy scalars to match the integral model) angular and linear kinetic energies, $\overline{\mathcal{K}}_i = \overline{\mathcal{K}}_i^{v} + \overline{\mathcal{K}}_i^{\omega}$. Thus, by applying the partial derivatives with respect to the joint-space velocities on $\overline{\mathcal{K}}_i$, we obtain the generalized inertia matrix contributions as $\overline{\mathbf{M}}_i = \overline{\mathbf{M}}_i^{\omega} + \overline{\mathbf{M}}_i^{v}$. Using the angular velocity Jacobian, $\overline{\mathbf{J}}_i^{\Omega}$ and the scalar coefficients derived in Section III-B2, we can derive $\overline{\mathbf{M}}_i^{\omega}$ as

$$\overline{\mathbf{M}}_i^{\omega} = I_{xx}\mathbb{T}_2 \begin{bmatrix} \beta_1^{\omega}\sigma_{11}^{\omega} & \beta_2^{\omega}\sigma_{12}^{\omega} \\ \beta_2^{\omega}{\sigma_{12}^{\omega}}^T & \beta_3^{\omega}\sigma_{22}^{\omega} \end{bmatrix} \tag{24}$$

where $\sigma_{11}^{\omega} = \left(\mathbf{J}_{i-1}^{\Omega}\overline{\mathbf{R}}_i\right)^T \mathbf{J}_{i-1}^{\Omega}\overline{\mathbf{R}}_i$, $\sigma_{12}^{\omega} = \left(\mathbf{J}_{i-1}^{\Omega}\overline{\mathbf{R}}_i\right)^T \overline{\mathbf{R}}_{i,\boldsymbol{q}_i^T}$, and $\sigma_{22}^{\omega} = \overline{\mathbf{R}}_{i,\boldsymbol{q}_i^T}^T \overline{\mathbf{R}}_{i,\boldsymbol{q}_i^T}$.

Equivalently, by applying the recursive form of the Jacobian in (15) and the energy scalars derived in Section III-B2, we can derive $\overline{\mathbf{M}}_i^{v}$ as

$$\overline{\mathbf{M}}_i^{v} = m_i \begin{bmatrix} \sigma_{11}^{v} & \sigma_{12}^{v} \\ {\sigma_{12}^{v}}^T & \sigma_{22}^{v} \end{bmatrix} \tag{25}$$

TABLE III
TERMS ASSOCIATED WITH (27) AND (28)

$$\eta_{11}^{\omega} = 2\beta_1^{\omega}\left(\mathbf{J}_{i-1}^{\Omega}\overline{\mathbf{R}}_i\right)^T\left(\mathbf{H}_{i-1}^{\Omega}\right)_h\overline{\mathbf{R}}_i$$
$$\eta_{12}^{\omega} = \beta_2^{\omega}\left\{\left(\mathbf{H}_{i-1}^{\Omega}\right)_h\overline{\mathbf{R}}_{i,\boldsymbol{q}_i}\right\}^T\overline{\mathbf{R}}_i$$
$$\eta_{11}^{\omega} = \mathbf{0}$$
$$\gamma_{11}^{\omega} = 2\beta_1^{\omega}\left(\mathbf{J}_{i-1}^{\Omega}\overline{\mathbf{R}}_{i,h}\right)^T\mathbf{J}_{i-1}^{\Omega}\overline{\mathbf{R}}_i$$
$$\gamma_{12}^{\omega} = \beta_2^{\omega}\left(\mathbf{J}_{i-1}^{\Omega}\overline{\mathbf{R}}_{i,\boldsymbol{q}_i,h}\right)^T\overline{\mathbf{R}}_i + \left(\mathbf{J}_{i-1}^{\Omega}\overline{\mathbf{R}}_{i,\boldsymbol{q}_i}\right)^T\overline{\mathbf{R}}_{i,h}$$
$$\gamma_{22}^{\omega} = 2\beta_3^{\omega}\overline{\mathbf{R}}_{i,\boldsymbol{q}_i,h}^T\overline{\mathbf{R}}_{i,\boldsymbol{q}_i^T}$$
$$\eta_{11}^{v} = 2\left(\mathbf{H}_{i-1}^{v}\right)_h^T\left(\mathbf{J}_{i-1}^{v} + \mathbf{J}_{i-1}^{\Omega}\overline{\boldsymbol{p}}_i\right) + 2{\mathbf{J}_{i-1}^{v}}^T\left(\mathbf{H}_{i-1}^{\Omega}\right)_h\overline{\boldsymbol{p}}_i +$$
$$2\beta_1^{v}\left(\mathbf{J}_{i-1}^{\Omega}\overline{\boldsymbol{p}}_i\right)^T\left(\mathbf{H}_{i-1}^{\Omega}\right)_h\overline{\boldsymbol{p}}_i$$
$$\eta_{12}^{v} = \left\{\left(\mathbf{H}_{i-1}^{v}\right)_h + \beta_2^{v}\mathbf{H}_{i-1}^{\Omega}\overline{\boldsymbol{p}}_i\right\}^T\overline{\boldsymbol{p}}_{i,\boldsymbol{q}_i^T}$$
$$\eta_{22}^{v} = \mathbf{0}$$
$$\gamma_{11}^{v} = 2{\mathbf{J}_{i-1}^{v}}^T\mathbf{J}_{i-1}^{\Omega}\overline{\boldsymbol{p}}_{i,h} + 2\beta_1^{v}\left(\mathbf{J}_{i-1}^{\Omega}\overline{\boldsymbol{p}}_{i,h}\right)^T\mathbf{J}_{i-1}^{\Omega}\overline{\boldsymbol{p}}_i$$
$$\gamma_{12}^{v} = \left(\mathbf{J}_{i-1}^{v} + \beta_2^{v}\mathbf{J}_{i-1}^{\Omega}\overline{\boldsymbol{p}}_i\right)^T\overline{\boldsymbol{p}}_{i,\boldsymbol{q}_i^T,h} + \beta_2^{v}\left(\mathbf{J}_{i-1}^{\Omega}\overline{\boldsymbol{p}}_{i,h}\right)^T\overline{\boldsymbol{p}}_{i,\boldsymbol{q}_i^T}$$
$$\gamma_{22}^{v} = 2\beta_3^{v}\overline{\boldsymbol{p}}_{i,\boldsymbol{q}_i^T,h}^T\overline{\boldsymbol{p}}_{i,\boldsymbol{q}_i^T}$$

where $\sigma_{11}^{v} = {\mathbf{J}_{i-1}^{v}}^T(\mathbf{J}_{i-1}^{v} + 2\mathbf{J}_{i-1}^{\Omega}\overline{\boldsymbol{p}}_i) + \beta_1^{v}(\mathbf{J}_{i-1}^{\Omega}\overline{\boldsymbol{p}}_i)^T\mathbf{J}_{i-1}^{\Omega}\overline{\boldsymbol{p}}_i$, $\sigma_{12}^{v} = \left(\mathbf{J}_{i-1}^{v} + \beta_2^{v}\mathbf{J}_{i-1}^{\Omega}\overline{\boldsymbol{p}}_i\right)^T\overline{\boldsymbol{p}}_{i,\boldsymbol{q}_i^T}$, and $\sigma_{22}^{v} = \beta_3^{v}\overline{\boldsymbol{p}}_{i,\boldsymbol{q}_i^T}^T\overline{\boldsymbol{p}}_{i,\boldsymbol{q}_i^T}$.

B. Coriolis and Centrifugal Force Matrix $\left(\overline{\mathbf{C}}_i\right)$

Using partial derivatives of $\overline{\mathbf{M}}_i$, the Christoffel symbols of the second kind are used to derive the $\overline{\mathbf{C}}_i$ elements as

$$\left[\overline{\mathbf{C}}_i\right]_{jk} = \frac{1}{2}\sum_{h=1}^{3i}\left(\left[\overline{\mathbf{M}}_i\right]_{kj,q_h} + \left[\overline{\mathbf{M}}_i\right]_{kh,q_j} - \left[\overline{\mathbf{M}}_i\right]_{hj,q_k}\right)\dot{q}_h. \tag{26}$$

Noting that $\overline{\mathbf{M}}_i = \overline{\mathbf{M}}_i^{\omega} + \overline{\mathbf{M}}_i^{v}$, by applying partial derivatives with respect to $h \in \boldsymbol{q}^i$, we get $\overline{\mathbf{M}}_{i,h} = \overline{\mathbf{M}}_{i,h}^{\omega} + \overline{\mathbf{M}}_{i,h}^{v}$. Hence, considering the variable with respect to which the partial derivation is carried out, we can obtain $\overline{\mathbf{M}}_{i,h}^{\omega}$ as

$$\overline{\mathbf{M}}_{i,h}^{\omega} = I_{xx}\mathbb{T}_2\begin{cases}\begin{bmatrix}\eta_{11}^{\omega} & \eta_{12}^{\omega}\\ {\eta_{12}^{\omega}}^T & \eta_{22}^{\omega}\end{bmatrix}, & h \in \boldsymbol{q}^{i-1}\\ \begin{bmatrix}\gamma_{11}^{\omega} & \gamma_{12}^{\omega}\\ {\gamma_{12}^{\omega}}^T & \gamma_{22}^{\omega}\end{bmatrix}, & h \in \boldsymbol{q}_i\end{cases} \tag{27}$$

where $(\mathbf{H}_{i-1}^{\Omega})_h = \mathbf{J}_{i-1,h}^{\Omega}$ is the submatrix of $\mathbf{H}_{i-1}^{\Omega}$ and the terms are listed in Table III.

Similarly, $\overline{\mathbf{M}}_{i,h}^{v}$ is given by

$$\overline{\mathbf{M}}_{i,h}^{v} = m_i\begin{cases}\begin{bmatrix}\eta_{11}^{v} & \eta_{12}^{v}\\ {\eta_{12}^{v}}^T & \eta_{22}^{v}\end{bmatrix}, & h \in \boldsymbol{q}^{i-1}\\ \begin{bmatrix}\gamma_{11}^{v} & \gamma_{12}^{v}\\ {\gamma_{12}^{v}}^T & \gamma_{22}^{v}\end{bmatrix}, & h \in \boldsymbol{q}_i\end{cases} \tag{28}$$

where $\left(\mathbf{H}_{i-1}^{v}\right)_h = \left(\mathbf{J}_{i-1}^{v}\right)_{,h}$ is the submatrix of $\mathbf{H}_{i-1}^{v}$ and the terms are listed in Table III.

Algorithm 1: Outline of the CoG-Based EoM Derivation via Recursive Lagrangian Formulation.

FOR i **FROM** 1 **TO** n **DO**
  compute $\boldsymbol{p}_i$, $\mathbf{R}_i$, $\overline{\boldsymbol{p}}_i$, $\overline{\mathbf{R}}_i$, and partial derivatives
  compute $\mathbf{M}_i = \mathbf{M}_i + (\mathbf{M}_i^{\omega} + \mathbf{M}_i^{v})$
  compute $\boldsymbol{G}_i = \boldsymbol{G}_i + (\boldsymbol{G}_i^{p} + \boldsymbol{G}_i^{e})$
  FOR h **FROM** 1 **TO** n **DO**
    compute $\mathbf{M}_{i,h}$
  update $\mathbf{J}_i^{v}$, $\mathbf{J}_i^{\omega}$, $\boldsymbol{p}^{\boldsymbol{i}}$, and $\mathbf{R}^i$
FOR i **FROM** 1 **TO** n **DO**
  compute $\mathbf{C}_i = f(\mathbf{M}_{i,h})$
SOLVE
  $\overline{\mathbf{M}}\ddot{\boldsymbol{q}} + \left(\overline{\mathbf{C}} + \mathbf{D}\right)\dot{\boldsymbol{q}} + \overline{\boldsymbol{G}} = \boldsymbol{\tau}$

C. Conservative Force Matrix $(\mathbf{G}_i)$

The total potential energy of a continuum section is $\mathcal{P}_i = \mathcal{P}_i^g + \mathcal{P}_i^e$, where $\mathcal{P}_i^g$ and $\mathcal{P}_i^e$ are gravitational and elastic potential energies. Therefore, $\boldsymbol{G}_i$ can be written as $\boldsymbol{G}_i = \boldsymbol{G}_i^g + \boldsymbol{G}_i^e$ [36]. For the ith section, $\mathcal{P}_i^g$ can be written as $\mathcal{P}_i^g = m_i\boldsymbol{g}^T\overline{\boldsymbol{p}}^i$. As there are no products of integrable terms, $\boldsymbol{G}_i^g$ is identical for both integral and CoG-based models and given by

$$\begin{aligned}\boldsymbol{G}_i^{gT} &= \left(m_i\boldsymbol{g}^T\overline{\boldsymbol{p}}^i\right)_{,(\boldsymbol{q}^i)^T}\\ &= m_i\boldsymbol{g}^T\mathbf{R}^{i-1}\left[\mathbf{J}_{i-1}^{v} + \mathbf{J}_{i-1}^{\Omega}\overline{\boldsymbol{p}}_i\ \overline{\boldsymbol{p}}_{i,\boldsymbol{q}_i^T}\right]\end{aligned} \tag{29}$$

where the derivation is included in Appendix G.

The elastic potential energy, $\mathcal{P}^e = \frac{1}{2}\boldsymbol{q}^T\mathbf{K}_e\boldsymbol{q}$, is independent of mass or the relative position in the task-space. Hence, similar to $\boldsymbol{G}_i^g$, $\boldsymbol{G}_i^e$ identical in both integral and CoG-based systems and could be readily formulated as

$$\boldsymbol{G}_i^e = \mathcal{P}_{i,\boldsymbol{q}_i}^e = \mathbf{K}_e\boldsymbol{q}_i. \tag{30}$$

D. Numerical Simulation Model

The EoM numerical model was implemented in MATLAB 2017a on a computer with Intel i7-4910MQ (2.9 GHz) and 32-GB RAM. The HTM was implemented in Maple 16 [45] symbolically and manipulated to derive the CoG-based terms and the partial derivatives thereof. Similarly, the kinematic terms of the ith section used for computing the forward kinematics [i.e., Jacobians given by (5) and (7) and Hessians given by (6) and (8)] were computed by making $\xi_i = 1$. Algorithm 1, implemented in the MATLAB Simulink environment, is used to numerically solve the EoM using the integrated ODE15s solver. Fig. 5(a) compares the CoG-based model against the integral dynamics model reported in [36], where the former is of $\mathcal{O}\left(n^2\right)$, whereas the latter is $\mathcal{O}\left(n^3\right)$. For a single-section system (three DoFs), both models show similar computation cost, but the numerical efficiency of the proposed model is evident for multisection continuum arms. The performance gain achieved by the proposed model relative to the integral dynamics model is plotted in Fig. 5(b). It can be seen that the CoG model is ideally suited for simulating dynamics of multisection continuum arms. The dynamic parameters and coefficients, such as $\mathbf{K}_i^e$ and $\mathbf{D}_i$, are

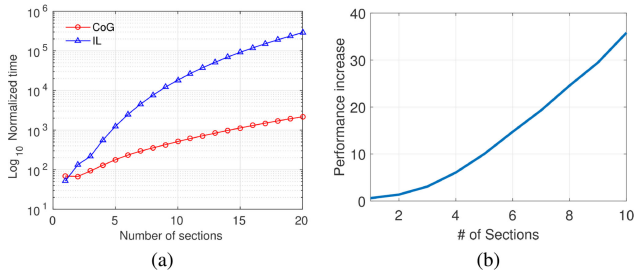

Fig. 5. (a) Time complexity comparison and (b) performance gain of CoG-based dynamics against integral Lagrangian dynamics as the number of continuum sections (i.e., DoF) increase.

difficult to measure or accurately estimate solely through physical and material properties. Therefore, such parameters were identified through an iterative system characterization process. In addition, input force τ is computed as $\tau = PA$, where P is the input pressure vector, and $A = 2.2 \times 10^{-4}\,\mathrm{m}^2$ is the PMA cross-sectional area. The reader is referred to [36] for a detailed discussion of the process including the information regarding the experimental setup and continuum arm shape measurement techniques.

V. Comparison to Experimental Results and Integral Dynamics

Fig. 1(a) shows the prototype continuum arm utilized in the following experiments. We use the data reported in [36] and compare the proposed CoG-based dynamics against the integral dynamics and the experimental results therein. Readers are referred to [36] for side-by-side visual comparison of resulting continuum arm motion.

The first experiment involves sectionwise actuation of all the sections on the $y = 0$ plane. The joint-space variables (physically the PMA's of continuum sections), l_{33}, l_{22}, and l_{11}, are supplied with 600, 500, and 500 kPa step pressure inputs at $t = 0$ s, $t = 3.2$ s, and $t = 7.55$ s, respectively. The EoM given in (23), derived using the proposed CoG-based approach, is the provided the same pressure input to simulate the forward dynamics. The simulation took 1.13 s to complete, which is 6.69 times faster than real time. The resultant joint-space trajectories are then applied to the kinematic model given by (23) to compute the associated tip task-space trajectories. The section tip coordinate task-space trajectories, measured using a two-camera setup [36] (illustrated in various shaped discrete markers), are then compared to the simulated task-space trajectories (drawn in solid lines) in Fig. 6. In addition, the task-space trajectories computed by the integral dynamics [36] are also included to compare the performance of the two approaches (shown in dotted lines). The errors between the experimental data versus CoG-based model and integral dynamics are also shown in each of the subplots for ease of comparison. It can be seen that the difference in errors and simulated results between the two numerical models is negligible. The aggregated error, plotted in the bottom subplot, shows the maximum error among the three tip positions and the mean of the position errors of all sections. It can be seen that the proposed model matches the integral dynamics proposed in [36].

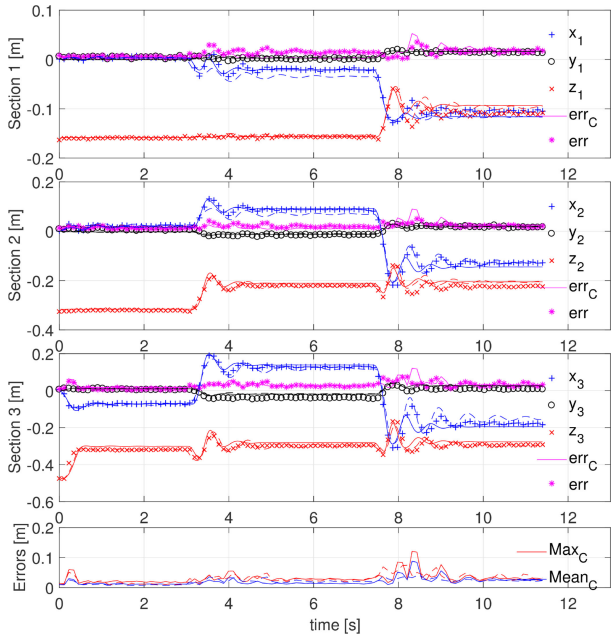

Fig. 6. Tip coordinate (X: blue, Y: black, and Z: red) trajectories of continuum sections for the first experiment. Experimental X, Y, and Z trajectories for each section tips are denoted by $+$, $\circ$, and $\times$ marks, respectively. Integral dynamic simulation results are shown in dashed (- -) lines, whereas CoG-based dynamic simulation results are shown in solid lines of the same colors. Tip trajectory plots include the position errors (Euclidean distance between experimental and simulation data) at each tip for integral dynamics (magenta * marks) and CoG-based dynamics (solid magenta lines). The mean (dashed lines)and maximum (solid lines) of the tip errors for the integral (blue) and CoG-based (red) dynamics are shown in the bottom plot.

Similar plots are generated for two further experiments detailed below.

The second experiment involves the actuation of the distal and mid section in two nonparallel bending planes, while the base section remains unactuated. Step pressure inputs of 300 and 500 kPa were applied to l_{23} at $t = 0$ s and l_{33} at $t = 3.3$ s, respectively. The resulting experimental and simulated task-space trajectories (using both integral dynamics and CoG-based dynamics) are shown in Fig. 7. The base section, though unactuated, deforms passively to balance the dynamic forces induced by the other moving sections and weight of the arm due to gravity, which is correctly modeled by both integral and CoG-based dynamic models. The numerical computation was 7.8 times faster than real time and completed within 0.89 s. Both models show comparable errors during the transient phase of the step response, but both models correctly simulate the steady-state dynamics afterward. The error in this experiment also varies during the step input transient stages, but section settles down quickly.

The third experiment extends the second and includes the actuation of the base section. The prototype and the dynamic model are provided pressure step inputs of 500, 300, and 300 kPa are, respectively, to actuators l_{33} at $t = 0$ s , l_{23} at $t = 2.55$ s, and l_{11} at $t = 5.05$ s and maintained during the experiment, and cause the continuum arm sections to deform in nonparallel planes. Fig. 8 compares the integral and CoG-based dynamics against the experimental results reported in [36]. The simulation only

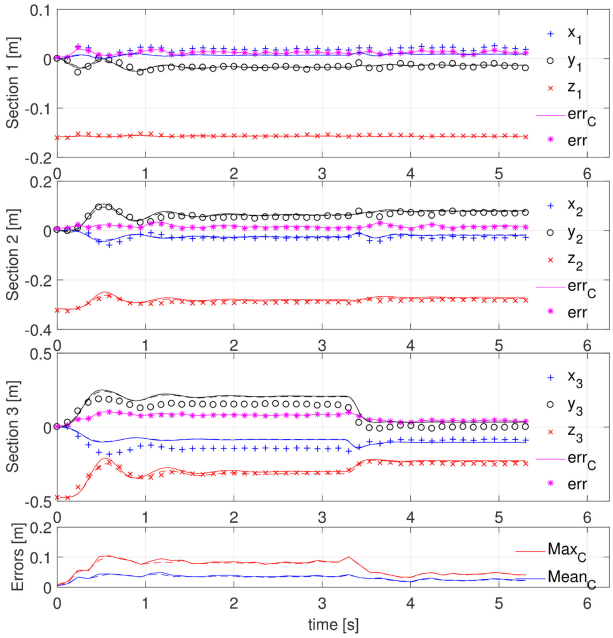

Fig. 7. Tip coordinate (X: blue, Y: black, and Z: red) trajectories of continuum sections for the second experiment. The legend is the same as Fig. 6.

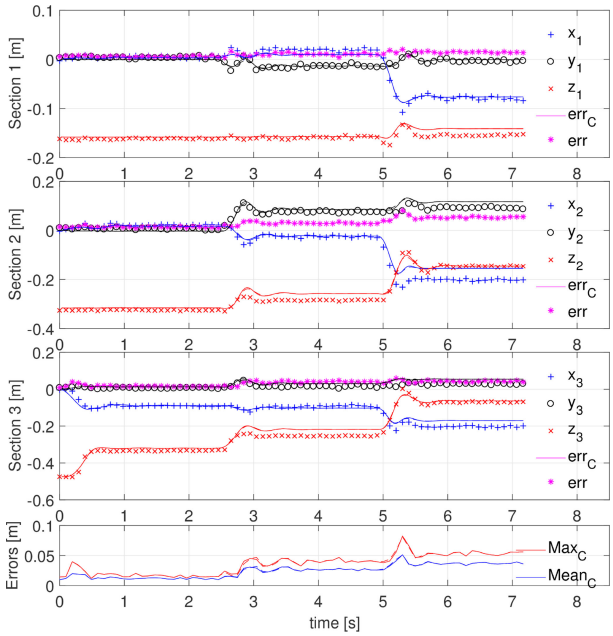

Fig. 8. Tip coordinate (X: blue, Y: black, and Z: red) trajectories of continuum sections for the third experiment. The legend is the same as Fig. 6.

took 1.3 s to complete this 7.9-s-long experiment, which is 7.3 times faster than real time. It can be seen that the CoG-based dynamics agrees with both the integral dynamics and experimental results. These experimental and empirical data demonstrate that the proposed numerically efficient CoG-based dynamic model for variable-length multisection continuum arms successfully simulates both the transient and steady-state dynamic behaviors well.

VI. Conclusion

Multisection continuum arms have strong potential for use in human-friendly spaces. Despite continued research, they have yet to make their mark outside the laboratory settings. A key reason for this is the lack of numerically efficient dynamic models that can be used in sub-real-time. Accuracy, numerical stability, and efficiency are critical for dynamic models to be used in dynamic control. Limited research has been conducted on physically accurate dynamic modeling of multisection continuum arm experimental validation thereof. In this paper, a novel CoG-based dynamic model was proposed. The work extended our prior work on CoG-based modeling of a single continuum section to derive a general model that can be used not only on arbitrarily long continuum arms, but also such robots of varying physical sizes. The results show that the model accommodates arbitrarily long variable-length multisection continuum arms and various length–radii combinations, considers both linear and angular kinetic energies at the CoGs of sections for more accuracy in energy computation, matches energy through a series of constant (for any variable-length multisection continuum arm) energy-shaping coefficients, derives the EoM terms recursively, attains $\mathcal{O}\left(n^2\right)$ complexity for continuous (nondiscretized) dynamic model for variable-length arms, and is six to eight times numerically efficient than real time for a three-section continuum arm model (suitable for implementing dynamic control schemes) and runs at 9.5 kHz. The model was experimentally validated on a three-section continuum arm and showed that results agree well with both the robot output and the integral dynamic models.

Appendix
Mathematical Derivations

A. Recursive Angular Body Velocity

$$\begin{aligned}\boldsymbol{\Omega}_i &= \mathbf{R}^{i^T}\dot{\mathbf{R}}^i \\ &= \left(\mathbf{R}^{i-1}\mathbf{R}_i\right)^T\left(\dot{\mathbf{R}}^{i-1}\mathbf{R}_i + \mathbf{R}^{i-1}\dot{\mathbf{R}}_i\right) \\ &= \mathbf{R}_i\left\{\left(\mathbf{R}^{i-1^T}\dot{\mathbf{R}}^{i-1}\right)\mathbf{R}_i + \left(\mathbf{R}^{i-1^T}\mathbf{R}^{i-1}\right)\dot{\mathbf{R}}_i\right\} \\ &= \mathbf{R}_i^T\left(\boldsymbol{\Omega}_{i-1}\mathbf{R}_i + \dot{\mathbf{R}}_i\right). \end{aligned} \tag{31}$$

B. Recursive Linear body Velocity

$$\begin{aligned}\boldsymbol{v}_i &= \mathbf{R}^{i^T}\dot{\boldsymbol{p}}^i \\ &= \left(\mathbf{R}^{i-1}\mathbf{R}_i\right)^T\left(\dot{\boldsymbol{p}}^{i-1} + \dot{\mathbf{R}}^{i-1}\mathbf{R}_i + \mathbf{R}^{i-1}\dot{\boldsymbol{p}}_i\right) \\ &= \mathbf{R}_i^T\left\{\left(\mathbf{R}^{i-1^T}\dot{\boldsymbol{p}}^{i-1}\right)\mathbf{R}_i + \left(\mathbf{R}^{i-1^T}\dot{\mathbf{R}}^{i-1}\right)\boldsymbol{p}_i \cdots \right. \\ &\quad \left. + \left(\mathbf{R}^{i-1^T}\mathbf{R}^{i-1}\right)\dot{\boldsymbol{p}}_i\right\} \\ &= \mathbf{R}_i^T\left(\boldsymbol{v}_{i-1} + \boldsymbol{\Omega}_{i-1}\boldsymbol{p}_i + \dot{\boldsymbol{p}}_i\right). \end{aligned} \tag{32}$$

C. Recursive Angular Body Velocity Jacobian

$$\begin{aligned}\mathbf{J}_i^{\Omega} &= \boldsymbol{\Omega}_{i,(\dot{\boldsymbol{q}}^i)^T} \\ &= \mathbf{R}_i^T \left(\boldsymbol{\Omega}_{i-1}\mathbf{R}_i + \dot{\mathbf{R}}_i\right)_{,(\dot{\boldsymbol{q}}^i)^T} \\ &= \mathbf{R}_i^T \left[\, \boldsymbol{\Omega}_{i-1,(\dot{\boldsymbol{q}}^{i-1})^T}\mathbf{R}_i \middle| \dot{\mathbf{R}}_{i,\dot{\boldsymbol{q}}_i^T} \,\right] \\ &= \mathbf{R}_i^T \left[\, \mathbf{J}_{i-1}^{\Omega}\mathbf{R}_i \middle| \mathbf{R}_{i,\boldsymbol{q}_i} \,\right]. \end{aligned} \tag{33}$$

D. Recursive Linear Body Velocity Jacobian

$$\begin{aligned}\mathbf{J}_i^{v} &= \boldsymbol{v}_{i,(\dot{\boldsymbol{q}}^i)^T} \\ &= \mathbf{R}_i^T \left(\boldsymbol{v}_{i-1} + \boldsymbol{\Omega}_{i-1}\boldsymbol{p}_i + \dot{\boldsymbol{p}}_i\right)_{,(\dot{\boldsymbol{q}}^i)^T} \quad \text{from (4)} \\ &= \mathbf{R}_i^T \left[\, \boldsymbol{v}_{i-1,(\dot{\boldsymbol{q}}^{i-1})^T} + \boldsymbol{\Omega}_{i-1,(\dot{\boldsymbol{q}}^{i-1})^T}\boldsymbol{p}_i \middle| \dot{\boldsymbol{p}}_{i,\dot{\boldsymbol{q}}_i^T} \,\right] \\ &= \mathbf{R}_i^T \left[\, \mathbf{J}_{i-1}^{v} + \mathbf{J}_{i-1}^{\Omega}\boldsymbol{p}_i \middle| \boldsymbol{p}_{i,\boldsymbol{q}_i^T} \,\right]. \end{aligned} \tag{34}$$

E. Recursive Angular Body Velocity Hessian

$$\begin{aligned}\mathbf{H}_i^{\Omega} &= \mathbf{J}_{i,\boldsymbol{q}^i}^{\Omega} \\ &= \left(\mathbf{R}_i^T \left[\, \mathbf{J}_{i-1}^{\Omega}\mathbf{R}_i \;\; \mathbf{R}_{i,\boldsymbol{q}_i^T} \,\right]\right)_{,\boldsymbol{q}^i} \\ &= \left[\begin{array}{c|c} \mathbf{R}_i^T \left(\mathbf{J}_{i-1,\boldsymbol{q}^{i-1}}^{\Omega}\right)\mathbf{R}_i & \mathbf{R}_{i,\boldsymbol{q}_i^T,\boldsymbol{q}^{i-1}} \\ \hline \begin{array}{c}\mathbf{R}_{i,\boldsymbol{q}_i}^T\mathbf{J}_{i-1}^{\Omega}\mathbf{R}_i\cdots \\ +\mathbf{R}_i^T\mathbf{J}_{i-1}^{\Omega}\mathbf{R}_{i,\boldsymbol{q}_i}\end{array} & \begin{array}{c}\mathbf{R}_{i,\boldsymbol{q}_i}^T\mathbf{R}_{i,\boldsymbol{q}_i^T}\cdots \\ +\mathbf{R}_i^T\mathbf{R}_{i,\boldsymbol{q}_i^T,\boldsymbol{q}_i}\end{array} \end{array}\right] \\ &= \left[\begin{array}{c|c} \mathbf{R}_i^T\mathbf{H}_{i-1}^{\Omega}\mathbf{R}_i & \mathbf{0} \\ \hline \begin{array}{c}\mathbf{R}_{i,\boldsymbol{q}_i}^T\mathbf{J}_{i-1}^{\Omega}\mathbf{R}_i\cdots \\ +\mathbf{R}_i^T\mathbf{J}_{i-1}^{\Omega}\mathbf{R}_{i,\boldsymbol{q}_i}\end{array} & \begin{array}{c}\mathbf{R}_{i,\boldsymbol{q}_i}^T\mathbf{R}_{i,\boldsymbol{q}_i^T}\cdots \\ +\mathbf{R}_i^T\mathbf{R}_{i,\boldsymbol{q}_i^T,\boldsymbol{q}_i}\end{array} \end{array}\right]. \end{aligned} \tag{35}$$

F. Linear Body Velocity Hessian

$$\begin{aligned}\mathbf{H}_i^{v} &= \mathbf{J}_{i,\boldsymbol{q}^i}^{v} \\ &= \left(\mathbf{R}_i^T \left[\, \mathbf{J}_{i-1}^{v} + \mathbf{J}_{i-1}^{\Omega}\boldsymbol{p}_i \middle| \boldsymbol{p}_i \,\right]\right)_{,\boldsymbol{q}^i} \\ &= \left[\begin{array}{c|c} \mathbf{R}_i^T \left(\mathbf{J}_{i-1,\boldsymbol{q}^{i-1}}^{v} + \mathbf{J}_{i-1,\boldsymbol{q}^{i-1}}^{\Omega}\boldsymbol{p}_i\right) & \left(\mathbf{R}_i^T\boldsymbol{p}_{i,\boldsymbol{q}_i^T}\right)_{,\boldsymbol{q}^{i-1}} \\ \hline \begin{array}{c}\mathbf{R}_{i,\boldsymbol{q}_i}^T\left(\mathbf{J}_{i-1}^{v} + \mathbf{J}_{i-1}^{\Omega}\boldsymbol{p}_i\right)\cdots \\ +\mathbf{R}_i^T\mathbf{J}_{i-1}^{\Omega}\boldsymbol{p}_{i,\boldsymbol{q}_i}\end{array} & \begin{array}{c}\mathbf{R}_{i,\boldsymbol{q}_i}^T\boldsymbol{p}_{i,\boldsymbol{q}_i^T}\cdots \\ +\mathbf{R}_i^T\boldsymbol{p}_{i,\boldsymbol{q}_i^T,\boldsymbol{q}_i}\end{array} \end{array}\right] \\ &= \left[\begin{array}{c|c} \mathbf{R}_i^T\left(\mathbf{H}_{i-1}^{v} + \mathbf{H}_{i-1}^{\Omega}\boldsymbol{p}_i\right) & \mathbf{0} \\ \hline \begin{array}{c}\mathbf{R}_{i,\boldsymbol{q}_i}^T\left(\mathbf{J}_{i-1}^{v} + \mathbf{J}_{i-1}^{\Omega}\boldsymbol{p}_i\right)\cdots \\ +\mathbf{R}_i^T\mathbf{J}_{i-1}^{\Omega}\boldsymbol{p}_{i,\boldsymbol{q}_i}\end{array} & \begin{array}{c}\mathbf{R}_{i,\boldsymbol{q}_i}^T\boldsymbol{p}_{i,\boldsymbol{q}_i^T}\cdots \\ +\mathbf{R}_i^T\boldsymbol{p}_{i,\boldsymbol{q}_i^T,\boldsymbol{q}_i}\end{array} \end{array}\right]. \end{aligned} \tag{36}$$

G. Conservative Force Vector, $(\boldsymbol{G}_i^g)$

$$\begin{aligned}\boldsymbol{G}_i^{gT} &= m_i g^T \left(\overline{\boldsymbol{p}}^i\right)_{,(\boldsymbol{q}^i)^T} \\ &= m_i g^T \overline{\mathbf{R}}^i \left\{ \overline{\mathbf{R}}^{iT} \left(\overline{\boldsymbol{p}}^i\right)_{,(\boldsymbol{q}^i)^T} \right\} \\ &= m_i g^T \overline{\mathbf{R}}^i \mathbf{J}_{i-1}^{v} \\ &= m_i g^T \left(\mathbf{R}^{i-1}\overline{\mathbf{R}}_i\right)\mathbf{R}_i^T \left[\mathbf{J}_{i-1}^{v} + \mathbf{J}_{i-1}^{\Omega}\boldsymbol{p}_i \middle| \mathbf{R}^{i-1}\boldsymbol{p}_{i,\boldsymbol{q}_i^T}\right] \\ &= m_i g^T \mathbf{R}^{i-1}\left(\overline{\mathbf{R}}_i\mathbf{R}_i^T\right)\left[\mathbf{J}_{i-1}^{v} + \mathbf{J}_{i-1}^{\Omega}\boldsymbol{p}_i \middle| \mathbf{R}^{i-1}\boldsymbol{p}_{i,\boldsymbol{q}_i^T}\right] \\ &= m_i g^T \mathbf{R}^{i-1}\left(\left[\, \mathbf{J}_{i-1}^{v} + \mathbf{J}_{i-1}^{\Omega}\overline{\boldsymbol{p}}_i \middle| \mathbf{R}^{i-1}\overline{\boldsymbol{p}}_{i,\boldsymbol{q}_i^T} \,\right]\right). \end{aligned} \tag{37}$$

REFERENCES

[1] D. Camarillo, C. Milne, C. Carlson, M. Zinn, and J. Salisbury, "Mechanics modeling of tendon-driven continuum manipulators," *IEEE Trans. Robot.*, vol. 24, no. 6, pp. 1262–1273, Dec. 2008.

[2] J. Wilson, D. Li, Z. Chen, and R. George, "Flexible robot manipulators and grippers: Relatives of elephant trunks and squid tentacles," in *Robots and Biological Systems: Towards a New Bionics?*. New York, NY, USA: Springer, 1993, pp. 475–494.

[3] R. Qi, A. Khajepour, W. W. Melek, T. L. Lam, and Y. Xu, "Design, kinematics, and control of a multijoint soft inflatable arm for human-safe interaction," *IEEE Trans. Robot.*, vol. 33, no. 3, pp. 594–609, Jun. 2017.

[4] M. Ivanescu, N. Popescu, and D. Popescu, "A variable length tentacle manipulator control system," in *Proc. IEEE Int. Conf. Robot. Autom.*, 2005, pp. 3274–3279.

[5] T. Mahl, A. Hildebrandt, and O. Sawodny, "A variable curvature continuum kinematics for kinematic control of the bionic handling assistant," *IEEE Trans. Robot.*, vol. 30, no. 4, pp. 935–949, Aug. 2014.

[6] F. Renda, M. Giorelli, M. Calisti, M. Cianchetti, and C. Laschi, "Dynamic model of a multibending soft robot arm driven by cables," *IEEE Trans. Robot.*, vol. 30, no. 5, pp. 1109–1122, Oct. 2014.

[7] N. Cheng *et al.*, "Design and analysis of a robust, low-cost, highly articulated manipulator enabled by jamming of granular media," in *Proc. IEEE Int. Conf. Robot. Autom.*, 2012, pp. 4328–4333.

[8] M. Cianchetti, T. Ranzani, G. Gerboni, I. De Falco, C. Laschi, and A. Menciassi, "Stiff-flop surgical manipulator: Mechanical design and experimental characterization of the single module," in *Proc. IEEE/RSJ Int. Conf. Intell. Robots Syst.*, 2013, pp. 3576–3581.

[9] Y. J. Kim, S. Cheng, S. Kim, and K. Iagnemma, "Design of a tubular snake-like manipulator with stiffening capability by layer jamming," in *Proc. IEEE/RSJ Int. Conf. Intell. Robots Syst.*, 2012, pp. 4251–4256.

[10] I. S. Godage, G. A. Medrano-Cerda, D. T. Branson, E. Guglielmino, and D. G. Caldwell, "Modal kinematics for multisection continuum arms," *Bioinspiration Biomimetics*, vol. 10, no. 3, 2015, Art. no. 035002.

[11] M. D. Grissom *et al.*, "Design and experimental testing of the octarm soft robot manipulator," *Proc. SPIE*, vol. 6230, 2006, Art. no. 62301F.

[12] R. Cieslak and A. Morecki, "Elephant trunk type elastic manipulator—A tool for bulk and liquid materials transportation," *Robotica*, vol. 17, no. 1, pp. 11–16, 1999.

[13] S. Neppalli *et al.*, "OctArm—A soft robotic manipulator," in *Proc. IEEE/RSJ Int. Conf. Intell. Robots Syst.*, Oct. 29–Nov. 2, 2007, p. 2569.

[14] T. Zheng *et al.*, "Model validation of an octopus inspired continuum robotic arm for use in underwater environments," *J. Mech. Robot.*, vol. 5, no. 2, 2013, Art. no. 021004.

[15] C. Laschi, M. Cianchetti, B. Mazzolai, L. Margheri, M. Follador, and P. Dario, "Soft robot arm inspired by the octopus," *Adv. Robot.*, vol. 26, no. 7, pp. 709–727, 2012.

[16] M. Cianchetti, M. Follador, B. Mazzolai, P. Dario, and C. Laschi, "Design and development of a soft robotic octopus arm exploiting embodied intelligence," in *Proc. IEEE Int. Conf. Robot. Autom.*, 2012, pp. 5271–5276.

[17] J. Burgner-Kahrs, D. C. Rucker, and H. Choset, "Continuum robots for medical applications: A survey," *IEEE Trans. Robot.*, vol. 31, no. 6, pp. 1261–1280, Dec. 2015.

[18] G. S. Chirikjian and J. W. Burdick, "Kinematically optimal hyper-redundant manipulator configurations," *IEEE Trans. Robot. Autom.*, vol. 11, no. 6, pp. 794–806, Dec. 1995.

[19] M. Hannan and I. Walker, "The 'elephant trunk' manipulator, design and implementation," in *Proc. IEEE/ASME Int. Conf. Adv. Intell. Mechatronics*, 2001, vol. 1, pp. 14–19.

[20] G. S. Chirikjian and J. W. Burdick, "The kinematics of hyper-redundant robot locomotion," *IEEE Trans. Robot. Autom.*, vol. 11, no. 6, pp. 781–793, Dec. 1995.

[21] G. S. Chirikjian and J. W. Burdick, "A modal approach to hyper-redundant manipulator kinematics," *IEEE Trans. Robot. Autom.*, vol. 10, no. 3, pp. 343–354, Jun. 1994.

[22] R. Kang, D. T. Branson, T. Zheng, E. Guglielmino, and D. G. Caldwell, "Design, modeling and control of a pneumatically actuated manipulator inspired by biological continuum structures," *Bioinspiration Biomimetics*, vol. 8, no. 3, 2013, Art. no. 036008.

[23] F. Renda, F. Boyer, J. Dias, and L. Seneviratne, "Discrete cosserat approach for multisection soft manipulator dynamics," *IEEE Trans. Robot.*, vol. 34, no. 6, pp. 1518–1533, Dec. 2018.
[24] K. Xu and N. Simaan, "Analytic formulation for kinematics, statics, and shape restoration of multibackbone continuum robots via elliptic integrals," *J. Mech. Robot.*, vol. 2, no. 1, 2010, Art. no. 011006.
[25] W. S. Rone and P. Ben-Tzvi, "Continuum robot dynamics utilizing the principle of virtual power," *IEEE Trans. Robot.*, vol. 30, no. 1, pp. 275–287, Feb. 2014.
[26] D. Trivedi, A. Lotfi, and C. D. Rahn, "Geometrically exact models for soft robotic manipulators," *IEEE Trans. Robot.*, vol. 24, no. 4, pp. 773–780, Aug. 2008.
[27] R. Featherstone, *Rigid Body Dynamics Algorithms*, vol. 49. Berlin, Germany: Springer, 2008.
[28] H. Mochiyama, "Hyper-flexible robotic manipulators," in *Proc. IEEE Int. Symp. Micro-NanoMechatronics Human Sci.*, 2006, pp. 41–46.
[29] B. A. Jones and I. D. Walker, "Kinematics for multisection continuum robots," *IEEE Trans. Robot.*, vol. 22, no. 1, pp. 43–55, Feb. 2006.
[30] E. Tatlicioglu, I. D. Walker, and D. M. Dawson, "Dynamic modelling for planar extensible continuum robot manipulators," in *Proc. IEEE Int. Conf. Robot. Autom.*, 2007, pp. 1357–1362.
[31] E. Tatlicioglu, I. D. Walker, and D. M. Dawson, "New dynamic models for planar extensible continuum robot manipulators," in *Proc. IEEE/RSJ Int. Conf. Intell. Robots Syst.*, 2007, pp. 1485–1490.
[32] I. S. Godage, E. Guglielmino, D. T. Branson, G. A. Medrano-Cerda, and D. G. Caldwell, "Novel modal approach for kinematics of multisection continuum arms," in *Proc. IEEE/RSJ Int. Conf. Intell. Robots Syst.*, 2011, pp. 1093–1098.
[33] I. S. Godage, D. T. Branson, E. Guglielmino, G. A. Medrano-Cerda, and D. G. Caldwell, "Shape function-based kinematics and dynamics for variable length continuum robotic arms," in *Proc. IEEE Int. Conf. Robot. Autom.*, 2011, pp. 452–457.
[34] I. S. Godage, D. T. Branson, E. Guglielmino, G. A. Medrano-Cerda, and D. G. Caldwell, "Dynamics for biomimetic continuum arms: A modal approach," in *Proc. IEEE Int. Conf. Robot. Biomimetics*, 2011, pp. 104–109.
[35] I. S. Godage, D. T. Branson, E. Guglielmino, and D. G. Caldwell, "Pneumatic muscle actuated continuum arms: Modelling and experimental assessment," in *Proc. IEEE Int. Conf. Robot. Autom.*, 2012, pp. 4980–4985.
[36] I. S. Godage, G. A. Medrano-Cerda, D. T. Branson, E. Guglielmino, and D. G. Caldwell, "Dynamics for variable length multisection continuum arms," *Int. J. Robot. Res.*, vol. 35, no. 6, pp. 695–722, 2016.
[37] R. Kang, D. T. Branson, E. Guglielmino, and D. G. Caldwell, "Dynamic modeling and control of an octopus inspired multiple continuum arm robot," *Comput. Math. Appl.*, vol. 64, no. 5, pp. 1004–1016, 2012.
[38] N. Giri and I. D. Walker, "Three module lumped element model of a continuum arm section," in *Proc. IEEE/RSJ Int. Conf. Intell. Robots Syst.*, 2011, pp. 4060–4065.
[39] W. Khalil, G. Gallot, and F. Boyer, "Dynamic modeling and simulation of a 3-D serial eel-like robot," *IEEE Trans. Syst., Man, Cybern. C, Appl. Rev.*, vol. 37, no. 6, pp. 1259–1268, Nov. 2007.
[40] I. S. Godage, R. Wirz, I. D. Walker, and R. J. Webster, "Efficient spatial dynamics for continuum arms," in *Proc. ASME Dyn. Syst. Control Conf.*, 2015, Art. no. V003T53A005.
[41] I. S. Godage, R. Wirz, I. D. Walker, and R. J. Webster, III,"Accurate and efficient dynamics for variable-length continuum arms: A center of gravity approach," *Soft Robot.*, vol. 2, no. 3, pp. 96–106, 2015.
[42] J. Li and J. Xiao, "Determining grasping configurations for a spatial continuum manipulator," in *Proc. IEEE/RSJ Int. Conf. Intell. Robots Syst.*, 2011, pp. 4207–4214.
[43] R. Webster and B. Jones, "Design and kinematic modeling of constant curvature continuum robots: A review," *Int. J. Robot. Res.*, vol. 29, no. 13, pp. 1661–1683, 2010.
[44] I. S. Godage and I. D. Walker, "Dual quaternion based modal kinematics for multisection continuum arms," in *Proc. IEEE Int. Conf. Robot. Autom.*, 2015, pp. 1416–1422.
[45] *Maple User Manual*, Maplesoft, Waterloo, ON, Canada, 2010.

Isuru S. Godage (S'10–M'13) received the B.Sc. Eng. (Hons.) degree in electronic and telecommunication engineering from the University of Moratuwa, Moratuwa, Sri Lanka, in 2007, and the Ph.D. degree in robotics, cognition, and interaction technologies from the Italian Institute of Technology–University of Genoa, Genoa, Italy, in 2013.

He is currently an Assistant Professor of Robotics with the School of Computing and the Director of the Robotics and Medical Engineering Laboratory, DePaul University, Chicago, IL, USA. Previously, he held an Adjoint Assistant Professorship with Vanderbilt University, and Postdoctoral Research Fellowships with Vanderbilt University and Clemson University. His research has been funded by the National Science Foundation. His research interests include design, modeling, and control of continuum and soft robots for manipulation and locomotion in applications related to search and rescue and healthcare applications.

Robert J. Webster, III (S'97–M'08–SM'14) received the B.S. degree in electrical engineering from Clemson University, Clemson, SC, USA, in 2002, and the M.S. and Ph.D. degrees in mechanical engineering from Johns Hopkins University, Baltimore, MD, USA, in 2004 and 2007, respectively.

In 2008, he joined the Faculty of Vanderbilt University, Nashville, TN, USA, where he is currently the Richard A. Schroeder Professor of Mechanical Engineering, Electrical Engineering, Otolaryngology, Neurological Surgery, and Urologic Surgery, and directs the Medical Engineering and Discovery Laboratory. He is a member of the Steering Committee with the Vanderbilt Institute in Surgery and Engineering, which brings together physicians and engineers to solve challenging clinical problems. He is a Founder and serves as the President of Virtuoso Surgical Inc., Nashville. His current research interests include surgical robotics, image-guided surgery, and continuum robotics.

Dr. Webster, III, was the recipient of the IEEE Robotics and Automation Society Early Career Award, the National Science Foundation CAREER Award, the Robotics Science and Systems Early Career Spotlight Award, the IEEE Volz Award, and the Vanderbilt Engineering Award for Excellence in Teaching. He is the Chair of the International Society for Optics and Photonics Image-Guided Procedures, Robotic Interventions, and Modeling Conference.

Ian D. Walker (S'84–M'85–SM'02–F'06) received the B.Sc. degree in mathematics from the University of Hull, Hull, U.K., in 1983, and the M.S. and Ph.D. degrees in electrical engineering from the University of Texas at Austin, Austin, TX, USA, in 1985 and 1989, respectively.

His research interests include biologically inspired and continuum robotics and architectural robotics.

Dr. Walker has served as the Vice-President for Financial Activities for the IEEE Robotics and Automation Society and as the Chair of the Space Automation and Robotics Technical Committee of the American Institute of Aeronautics and Astronautics. He has also served on the Editorial Boards of the IEEE TRANSACTIONS ON ROBOTICS, IEEE TRANSACTIONS ON ROBOTICS AND AUTOMATION, the *International Journal of Robotics and Automation*, the IEEE ROBOTICS AND AUTOMATION MAGAZINE, and the *International Journal of Environmentally Conscious Design and Manufacturing*. He currently serves on the Editorial Board of *Soft Robotics*.